

# INTERSTELLAR FLOW AND TEMPERATURE DETERMINATION WITH *IBEX*: ROBUSTNESS AND SENSITIVITY TO SYSTEMATIC EFFECTS

E. MÖBIUS<sup>1</sup>, M. BZOWSKI<sup>2</sup>, P. C. FRISCH<sup>3</sup>, S. A. FUSELIER<sup>4,5</sup>, D. HEIRTZLER<sup>1</sup>, M. A. KUBIAK<sup>2</sup>, H. KUCHAREK<sup>1</sup>, M. A. LEE<sup>1</sup>,  
T. LEONARD<sup>1</sup>, D. J. MCCOMAS<sup>4,5</sup>, N. A. SCHWADRON<sup>1</sup>, J. M. SOKÓŁ<sup>2</sup>, P. SWACZYNA<sup>2</sup>, AND P. WURZ<sup>6</sup>

<sup>1</sup>Space Science Center and Department of Physics, University of New Hampshire, Durham, NH 03824, USA

<sup>2</sup>Space Research Centre, Polish Academy of Sciences, Warsaw, Poland

<sup>3</sup>Dept. Astronomy and Astrophysics, University of Chicago, Chicago, IL 60637, USA

<sup>4</sup>Southwest Research Institute, San Antonio, TX, USA

<sup>5</sup>University of Texas, San Antonio, TX, USA

<sup>6</sup>Physikalisches Institut, Universität Bern, Bern, Switzerland

Received 2015 May 9; accepted 2015 June 19; published 2015 October 20

## ABSTRACT

The *Interstellar Boundary Explorer* (*IBEX*) samples the interstellar neutral (ISN) gas flow of several species every year from December through late March when the Earth moves into the incoming flow. The first quantitative analyses of these data resulted in a narrow tube in four-dimensional interstellar parameter space, which couples speed, flow latitude, flow longitude, and temperature, and center values with approximately  $3^\circ$  larger longitude and  $3 \text{ km s}^{-1}$  lower speed, but with temperatures similar to those obtained from observations by the *Ulysses* spacecraft. *IBEX* has now recorded six years of ISN flow observations, providing a large database over increasing solar activity and using varying viewing strategies. In this paper, we evaluate systematic effects that are important for the ISN flow vector and temperature determination. We find that all models in use return ISN parameters well within the observational uncertainties and that the derived ISN flow direction is resilient against uncertainties in the ionization rate. We establish observationally an effective *IBEX*-Lo pointing uncertainty of  $\pm 0.18$  in spin angle and confirm an uncertainty of  $\pm 0.1$  in longitude. We also show that the *IBEX* viewing strategy with different spin-axis orientations minimizes the impact of several systematic uncertainties, and thus improves the robustness of the measurement. The Helium Warm Breeze has likely contributed substantially to the somewhat different center values of the ISN flow vector. By separating the flow vector and temperature determination, we can mitigate these effects on the analysis, which returns an ISN flow vector very close to the *Ulysses* results, but with a substantially higher temperature. Due to coupling with the ISN flow speed along the ISN parameter tube, we provide the temperature  $T_{\text{VISN}\infty} = 8710 + 440/-680 \text{ K}$  for  $V_{\text{VISN}\infty} = 26 \text{ km s}^{-1}$  for comparison, where most of the uncertainty is systematic and likely due to the presence of the Warm Breeze.

*Key words:* ISM: atoms – ISM: clouds – ISM: kinematics and dynamics – Sun: heliosphere

## 1. INTRODUCTION

Due to the Sun’s motion relative to its environment, the neutral gas component of the Local Interstellar Cloud (LIC) is accessible to in situ diagnostics in the form of an interstellar wind through the solar system. UV backscatter observations of H (Bertaux & Blamont 1971; Thomas & Krassa 1971; Adams & Frisch 1977) and He (Weller & Meier 1974; Ajello 1978) have been exploited, followed by pickup ion detection (Möbius et al. 1985; Gloeckler et al. 1992) and the direct measurements of interstellar neutral (ISN) He (Witte et al. 1996). A concerted attempt to combine results from these different optical and in situ methods led to a set of preliminary LIC consensus parameters (Möbius et al. 2004) and the conclusion that neutral gas observations (Witte 2004) should provide the distribution function of the ISN flow in the most detail. Early analysis of ISN flow observations with the *Interstellar Boundary Explorer* (*IBEX*; Bzowski et al. 2012; Möbius et al. 2012) resulted in a narrow tube of coupled ISN flow parameters that relates the speed  $V_{\text{ISN}\infty}$ , flow latitude  $\beta_{\text{ISN}\infty}$ , temperature  $T_{\text{ISN}\infty}$ , and the flow longitude  $\lambda_{\text{ISN}\infty}$ , whose center value differed by about  $3^\circ$ , with a flow speed lower by about  $3 \text{ km s}^{-1}$  but with the same temperature as found with *Ulysses* GAS (Witte 2004). One edge of the  $1\sigma$  uncertainty range along the *IBEX* parameter tube almost encompassed the same flow velocity vector, but with a much higher temperature. McComas et al. (2012) provided a

synthesis of the two analysis methods applied to the *IBEX*-Lo observations. They also suggested that there was no strong shock in front of the heliopause because of the reduced flow speed and higher interstellar magnetic field strength based on *IBEX* ribbon observations (Schwadron et al. 2011). This suggestion alone has led to a number of papers debating what kind of interface there might be between the interstellar medium and the heliosphere (Fuselier & Cairns 2013; Zank et al. 2013; Zieger et al. 2013; Scherer & Fichtner 2014). In addition, a small difference in the ISN flow direction has a strong influence on the orientation of the  $B_{\text{ISM}}-V_{\text{ISN}\infty}$  plane (Bzowski et al. 2012; Möbius et al. 2015) which, according to global heliospheric models, controls the shape of the heliosphere and the deflection of the plasma flow around the heliosphere (e.g., Opher et al. 2007; Pogorelov et al. 2009). Triggered by the intriguing possibility that the interstellar gas flow vector might be variable on observable timescales, Frisch et al. (2013) compiled all of the published determinations of the helium flow vector direction, starting from the early observations in the 1970s through today, and performed a statistical analysis. The result suggested that a change over time was more likely than a constant flow direction, and this suggestion has been debated (Lallement & Bertaux 2014). Further exploring the possibility of short-term temporal variations in the interstellar medium, Frisch et al. (2015) rebutted technical criticisms and discussed various possible change scenarios

rooted in the dynamic structure of the local medium and interstellar turbulence.

With such profound consequences, further detailed analysis of the observations that led to the potentially different results is clearly needed. Several groups have re-analyzed the *Ulysses* GAS observations, including observations during the last fast latitude scan of *Ulysses* in 2007, which had not been analyzed previously (Bzowski et al. 2014; Katushkina et al. 2014; Wood et al. 2015b). These analyses found a flow vector very close to the original *Ulysses* GAS results, but with a significantly higher temperature (Bzowski et al. 2014; Wood et al. 2015b) than reported by Witte (2004). Meanwhile, six years of ISN flow data with different pointings of the *IBEX* satellite have been accumulated. Two very recent analyses based on comparing *IBEX* data with our analytic model (Leonard et al. 2015) and using those results in combination with Warsaw test particle simulations (McComas et al. 2015a) provided a reevaluation of the *IBEX* ISN flow vector. They gave a direction and speed much closer to the *Ulysses* results, but with temperatures even higher than reported by Bzowski et al. (2014) and Wood et al. (2015b) for the *Ulysses* observations.

This paper is part of a Special Issue on *IBEX* ISN flow measurements, for which McComas et al. (2015b) provide an overview. The task at hand is to reduce the uncertainties of the *IBEX* observations and to find out what might have pulled the *IBEX* results toward a different center flow vector in the early analysis. To this end, we study how a combination of different analysis methods (Bzowski et al. 2012; Möbius et al. 2012) and an optimized variation of the *IBEX* pointing strategy (Möbius et al. 2015; Leonard et al. 2015) can be exploited to substantially improve the ISN flow and temperature results. We discuss a variety of systematic effects and uncertainties associated with the determination of the ISN flow vector and temperature from the *IBEX* observations. Among these, we revisit the absolute pointing of *IBEX*-Lo, for which the collimator boresight direction had been related to an absolute astronomical reference with an accuracy of  $\pm 0^\circ.1$  through the use of the *IBEX*-Lo star sensor (Hond et al. 2012). However, there is still a potential small asymmetry in the *IBEX*-Lo field of view (FOV) due to the asymmetric conversion surface efficiency, which leads to a somewhat larger uncertainty in the ISN flow vector. We include this and other remaining uncertainties in a broad discussion of the systematic effects and related uncertainties for the analysis method used by Möbius et al. (2012) and Leonard et al. (2015), followed by a discussion of why the *IBEX* observations might have led to noticeably different results for the ISN gas flow direction than previously observed. This study is complementary to the paper by Swaczyna et al. (2015), who discuss related systematic effects, specifically the analysis with the Warsaw Test Particle Model (WTPM; Bzowski et al. 2012, 2015; Sokół et al. 2015b). Our analysis substantiates that the presence of a secondary ISN He component, dubbed the Warm Breeze (Kubiak et al. 2014), perhaps in connection with a different observer location in the heliosphere, may have provided an important source of systematic uncertainty in previous analyses. Also, a remaining hidden dependence on the spin-axis orientation in the analytic expansion model (Lee et al. 2012, 2015) may have contributed, as was recently demonstrated by Leonard et al. (2015). In our new analysis of the contributing systematic effects, we find that the current

suite of ISN flow models and observations using an extended *IBEX* pointing strategy (Möbius et al. 2015) results in a robust solution for the ISN flow vector and temperature. In this solution, several systematic effects partially compensate for each other. We connect our evaluation of systematic uncertainties of the flow vector with two new studies. Schwadron et al. (2015) use an analytic full integration model to evaluate independently the ISN flow vector, and the paper by Lee et al. (2015) contains the description of the latest version of the analytic expansion model. Finally, we report on the ISN flow He temperature, its systematic effects, and uncertainties.

The paper is organized as follows. Section 2 briefly describes the *IBEX* mission, instrumentation, and observation and data selection relevant to the ISN flow determination. Section 3 describes the effects that influence the pointing accuracy. Section 4 contains the analysis methods, along with associated systematic uncertainties and their influence on the analysis results. Section 5 describes how the ISN temperature is determined from the angular width of the ISN flow distribution over the entire observation range with all associated statistical and systematic errors that follow from the previous sections. Section 6 is devoted to effects that may depend on the observer location in the heliosphere, and thus focuses on the observational differences between *IBEX* and *Ulysses* vantage points, with an emphasis on the secondary ISN distribution. Section 7 contains a discussion and summary of the results.

## 2. INSTRUMENTATION, OBSERVATION STRATEGY, AND DATA SELECTION

The *IBEX* spacecraft was launched in 2008 October and subsequently rose into a highly elliptical Earth orbit with an apogee of about  $50 R_E$ . Its science goals are to discover the global interaction between the heliosphere and the interstellar medium, and to sample the neutral interstellar wind through the solar system. The *IBEX* viewing geometry provides for observation of the ISN flow when it arrives nearly tangential to the Earth's orbit with sufficiently high energy when moving into the oncoming flow from late December through late March each year.

### 2.1. Overview of the *IBEX* Mission

*IBEX* was designed to observe heliospheric and interstellar energetic neutral atoms (ENAs) with as little interference from the terrestrial and magnetospheric background as possible. This Small Explorer (McComas et al. 2009) carries two single-pixel high-sensitivity ENA cameras, *IBEX*-Hi (Funsten et al. 2009) and *IBEX*-Lo (Fuselier et al. 2009). Their FOVs point radially outward in two opposite directions, and their combined energy range is 10–6000 eV with overlap between 300 and 2000 eV. *IBEX* is a roughly Sun-pointing, spinning satellite, whose spin axis is re-oriented toward the Sun after the completion of each 7–8 day orbit (2009–2011) and after each  $\approx 4.5$  day ascending and descending orbit arc (after 2011 June, McComas et al. 2011). Complete full-sky ENA maps are obtained with a resolution of the  $7^\circ$  FWHM sensor FOV every six months. *IBEX* samples heliospheric and interstellar ENA distributions at 1 AU in a plane that is approximately perpendicular to the Earth–Sun line. This is equivalent to observing these ENAs at the perihelia of their trajectories, independent of their flow direction at infinity.

## 2.2. *IBEX-Lo* Sensor

The *IBEX-Lo* sensor was optimized for the observation of the ISN gas flow of several species, while at the same time measuring ENAs in the energy range 10–2000 eV from the heliospheric boundary (Fuselier et al. 2009). *IBEX-Lo* uses a large area collimator to define the 7° FWHM FOV. Negatively biased rejection rings and a positive potential at the collimator are designed to repel electrons and ions, allowing only neutral atoms and photons to enter the sensor. While the electron rejection works as designed, the positive potential cannot be applied to the collimator. However, an additional internal deflection of incoming ions behind the *IBEX-Lo* collimator still prevents all ions with energies <200 eV from reaching the conversion surface, with partial rejection capability between 200 and 1000 eV. Neutral atoms (and ions >200 eV) that pass the collimator reach the conversion surface where a small fraction is converted to negative ions. These negative ions are selected for energy/charge within eight logarithmically spaced energy steps by an electrostatic analyzer (ESA), which also rejects any neutrals and positive ions. Serrations and blackening of the analyzer surfaces also efficiently suppress photons and secondary electrons (Wieser et al. 2007). After a +16 kV (+7 kV after July 2012) post-acceleration, negative ions are analyzed for their mass in a two-section time-of-flight (TOF) spectrograph. Triple coincidence conditions very effectively reject nearly all background (Möbius et al. 2008).

The central electronics unit (CEU) sorts the pulse height events based on their coincidence condition (giving triple coincidence events highest priority) and inserts a time-tag (counting time from each spin pulse). Events identified as H and O by the TOF spectrograph are sorted into 6° bin angle histograms for each energy step (for details see Fuselier et al. 2009).

While the *IBEX-Lo* TOF spectrograph determines the mass of incoming neutral atoms directly for those species (e.g., H and O) that are converted to negative ions, noble gases, such as He and Ne, do not effectively produce negative ions or produce none at all (Smirnov 1982). They still generate sputtered negative ions (H, C, and O) from the conversion surface, which are detected and identified in the *IBEX-Lo* TOF spectrograph (Wurz et al. 2008; Möbius et al. 2009a). The *IBEX-Lo* sensor was calibrated in the laboratory for its response using He and Ne at a variety of energies (Fuselier et al. 2009; Möbius et al. 2009b). Thus, the observed ratios of H, C, and O are used to infer the identity of the noble gas atoms (He or Ne), relevant here for ISN He. Sputtered ions generate a broad energy distribution that starts below the incoming energy of the neutral atom and extends to very low energies (Möbius et al. 2012), which results in a very flat energy response to the He ISN flow distribution. However, sputtering has a low energy cut-off that is relevant for potential observations of the ISN flow in fall, when the spacecraft and Earth are receding from the ISN flow (Galli et al. 2015; Sokół et al. 2015a), and for low-energy atoms from the Warm Breeze (Kubiak et al. 2014).

Because the original energy of the ISN He atoms cannot be determined, the geometry of the Keplerian trajectory from infinity to 1 AU in the Sun’s gravitational field is used to deduce the flow vector at infinity (Bzowski et al. 2012; Lee et al. 2012, 2015; Kubiak et al. 2014; Schwadron et al. 2015; Sokół et al. 2015b). This requires knowledge of the direction of the incoming neutral atoms at the point of observation, and thus

the exact pointing of *IBEX-Lo*, which will be discussed further in Section 3.

## 2.3. Data Selection

The selection of the interstellar gas flow observations for analysis follows the same criteria described in Möbius et al. (2012), which we briefly summarize below for completeness. An ISN list is generated for each ISN flow season, which is the basis for the data selection and analysis. Excluded from this list are time periods when the following conditions apply.

1. *IBEX* is close to the magnetosphere and *IBEX-Lo* observes significant count rates of magnetospheric ENAs and ions based on observations away from the ISN flow.
2. The Moon is in the *IBEX* FOV. These times are taken from the ISOC command files, which contain special commanding for the star sensor during these times.
3. The electron rates for *IBEX-Lo* are high. These times are identified in the *IBEX-Lo* TOF count rates when the otherwise very stable base count rate outside the ISN flow direction is exceeded by more than a factor of 1.6 (safely above any stochastic fluctuations of the base count rate, but low enough to indicate significant increases). This criterion also independently eliminates any time periods with contamination by magnetospheric ENAs, which lead to similar rate increases.
4. The star tracker function has been impaired by bright sources, such as the Earth or the Moon near its FOV. This would affect the precise determination of the ISN peak location and width in latitude, and thus is excluded from the analysis.

In a first analysis step, the angular ISN flow distributions are fit to a Gaussian distribution that includes an adjustable constant background as one of the parameters. The level of this background is typically <1/450, or at least <1/125, of the peak rate (Leonard et al. 2015). This level ensures that any background is at most a small contribution to the apparent ISN flow signal.

In addition, we exclude observations at ecliptic longitudes  $\lambda_{\text{Obs}} < 115^\circ$  (*IBEX* orbits equivalent to orbit 13 or lower in 2009) and ecliptic longitudes  $\lambda_{\text{Obs}} > 160^\circ$  (*IBEX* orbits equivalent to orbit 20 or higher in 2009) from the ISN flow vector analysis. The former condition minimizes the influence of the Warm Breeze on the results. Because of the importance of this effect and its apparently different impact on flow peak location and width, we discuss its effects in more detail in Sections 5 and 6. The latter condition also makes the influence of the H ISN flow (Saul et al. 2012; Schwadron et al. 2013) on the He observations negligible.

## 3. ACCURACY OF *IBEX-LO* POINTING AND OF THE ISN FLOW DIRECTION NEAR EARTH

When comparing the *IBEX* results for the ISN flow direction to those obtained with *Ulysses* GAS, it is important to evaluate how accurate the knowledge of the absolute pointing relative to astronomical coordinates can be achieved with both instruments and how the incoming flow might be affected by the location of the spacecraft. As for the first point, the collimator boresight direction of the *IBEX-Lo* sensor was related to an absolute astronomical reference with an accuracy of  $\pm 0^\circ.1$  through the *IBEX-Lo* star sensor (Hfond et al. 2012). However,

the effective sensor pointing could still deviate from the collimator pointing due to an asymmetric conversion surface efficiency. This potential asymmetry is addressed in Section 3.1 and combined with the known absolute pointing accuracy in Section 3.2. The refined determination of the *IBEX* spin-axis orientation for each orbit (Swaczyna et al. 2015) is included in the data sets and any remaining uncertainties are negligible compared to the constant pointing uncertainty described here. Potential effects from the vicinity of the Earth are addressed in Section 3.3 based on the analysis in Kucharek et al. (2015).

### 3.1. High- and Low-resolution Cross-calibrations

Figure 1 shows a schematic cross-sectional view of the *IBEX*-Lo sensor along with a top view of the sensor. *IBEX*-Lo is subdivided into three low- (angular) resolution (Lo-Res, or large geometric factor) quadrants and a high- (angular) resolution (Hi-Res, or small geometric factor) quadrant, with different orientation relative to the spacecraft spin axis.

As shown in Figure 1, a notable variation of the collection efficiency as a function of incidence angle relative to the plane of the conversion surface and location of incidence may lead to a deviation of the effective sensor pointing. The expected offset relative to the collimator boresight is toward the sensor central axis. As has been shown by Wahlström et al. (2008), the fraction of ions that are scattered isotropically as opposed to specular reflection when emerging from the conversion surface increases nonlinearly with increasing incidence angle. The *IBEX*-Lo ion optics collect negative ions from the conversion surface more effectively if they specularly reflect off the surface and if they emerge from locations closer to the ESA (Wieser et al. 2007). Consequently, ENAs that arrive at the conversion surface with a larger incidence angle (dashed lines in Figure 1) and on average, farther away from the ESA are transmitted to the TOF section with lower efficiency than ENAs that arrive at a shallower incidence angle (solid lines in Figure 1). Therefore, this angular variation in transmission efficiency over the collimator FOV (solid black triangle in the inset) modifies the effective *IBEX*-Lo FOV, as indicated by the gray shaded triangle in the inset. The expected shift in the effective boresight direction is along the radial direction for each quadrant of the annular collimator aperture. Thus, for a rotationally symmetric sensor, the effect would cancel to the extent that the overall sensor transmission efficiency is uniform over the annulus. However, with three low angular resolution quadrants (Lo-Res) and one high-resolution quadrant (Hi-Res) as shown in the bottom panel of Figure 1 (labeled Front View), *IBEX*-Lo is symmetric along the spin axis, but may exhibit an asymmetry in spin phase.

The potential offset from the collimator boresight in the spin direction is determined in flight through a special sensor operation. *IBEX*-Lo is operated either with all quadrants simultaneously or only the high-resolution quadrant turned on (Fuselier et al. 2009). When only the high-resolution section is operating, *IBEX*-Lo measures at high angular resolution ( $3.5^\circ$  FWHM), albeit with a greatly reduced geometric factor (by a factor of  $\approx 12$ ). With all of the quadrants operating simultaneously, *IBEX*-Lo measures at standard angular resolution ( $7^\circ$  FWHM) and full geometric factor. To determine primarily the difference in geometric factors for the two angular resolutions and to assess the influence of different particle rates on the *IBEX*-Lo data system, the sensor has been operated in a so-called cross-calibration mode. In this mode, *IBEX*-Lo is

switched periodically every 96 spins between the two angular resolutions, where high resolution is used for 84 spins and low resolution only for 12 spins (at a 7:1 ratio commensurate with an 8 energy step sensor cycle). If the angle-dependent collection efficiency for the negative ions leads to a noticeable asymmetry, then the resulting deviation in the boresight should be in the opposite direction for the low- and high-resolution quadrants (Figure 1), and thus be visible in a direct comparison. Therefore, in the following, we use cross-calibration observations that were performed for orbit 115 in 2011 and orbits 153b, 154a and b, and 156a in 2012 during the ISN flow observation season. In essence, we use the ISN flow as a calibration beam for this analysis. Repeated switching between the two sensor settings ensures that potential changes in the interstellar flow do not interfere with the comparison of the otherwise simultaneous observations.

Figure 2 shows the latitudinal angular distribution of the ISN flow during orbit 154b obtained with the high-resolution section (blue) and the full *IBEX*-Lo sensor (red). As in the ISN flow analysis by Möbius et al. (2012) and Bzowski et al. (2012), the observations are accumulated over  $6^\circ$  sectors for which the absolute flux corrected *IBEX*-Lo histograms are used (Möbius et al. 2012; Leonard et al. 2015). This is needed for both data sets because the particle rate that exceeds the transmission capability of the sensor interface and telemetry is mostly due to background events not used in the analysis, but which load the interface (Swaczyna et al. 2015).

The results of all cross-calibration observations from 2011 to 2012 are compiled in Figure 3. The differences in the derived peak position between individual high and low measurements show some variability between  $0.05^\circ$  and  $0.5^\circ$  at most. Propagating the statistical uncertainties for all of the individual measurements, a weighted average of the difference between the high- and low-resolution peak values is obtained, along with the standard error. We find  $0.03^\circ \pm 0.15^\circ$ , or no significant difference in the pointing between the high and low angular resolution quadrants. Rather than a difference, we establish a pointing uncertainty for the combined *IBEX*-Lo FOV relative to the geometrically established collimator boresight of  $\pm 0.15^\circ$  in spin phase.

### 3.2. Combined Absolute Pointing Accuracy

Hond et al. (2012) established an absolute pointing uncertainty relative to the astronomical coordinate system as set by star positions and, simultaneously, relative to the *IBEX* star tracker, of  $\pm 0.1^\circ$  in ecliptic longitude and latitude. The uncertainty found in Section 3.1 and the absolute astronomical pointing uncertainty are two independent uncertainties. Therefore, the combined *IBEX*-Lo pointing uncertainty in spin phase, and thus in ecliptic latitude relative to astronomical coordinates, contains the two added in quadrature which results in  $\Delta\psi' = \pm 0.18^\circ$ . Because the sensor configuration is symmetric along the spin axis, we retain  $\Delta\lambda = \pm 0.1^\circ$  from Hond et al. (2012) as uncertainty in ecliptic longitude.

### 3.3. Potential Earth Influence on the ISN Flow

Because *IBEX* observes the ISN flow from locations close to the Earth, a potential gravitational influence of the Earth on the flow direction cannot be excluded a priori. Kucharek et al. (2015) treat this problem in a more general context. They demonstrate that this influence may become important for

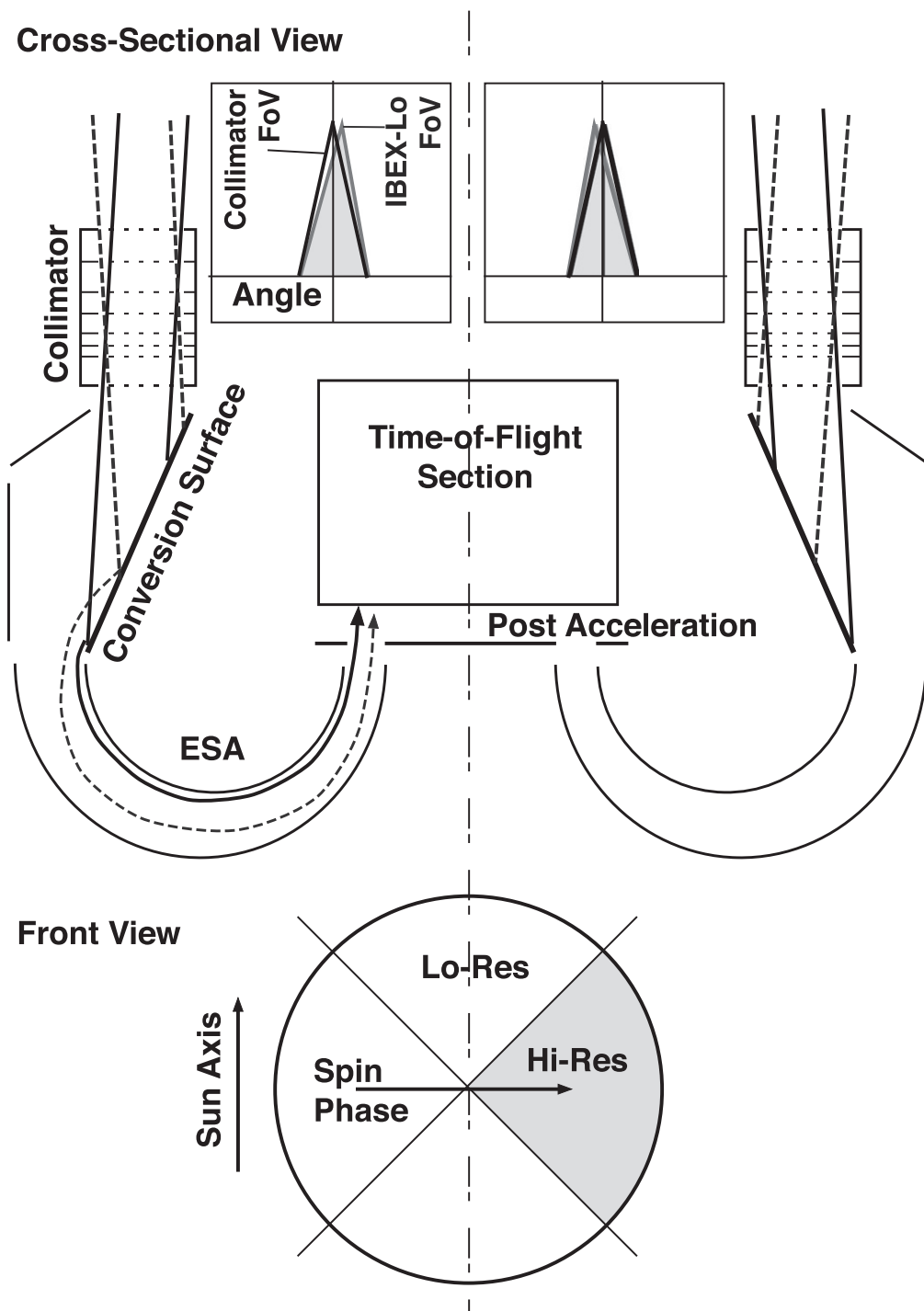


**Figure 1.** Schematic cross-sectional view (top) and front view of *IBEX-Lo* (bottom) in relation to spin axis and phase. Typical ENA trajectories are shown with high transmission efficiency (solid black lines) and low efficiency (dashed gray lines). The two insets show the collimator FOV (black triangle) and the effective FOV (gray shaded triangle).

observations in the fall when the ISN flow overtakes the Earth at substantially lower relative speed, but for all *IBEX* observations in spring it is negligible compared with the overall uncertainty budget, as we briefly summarize below.

For the ISN flow vector, the potential deflection is important in two planes that are depicted in Figure 4. During the spring ISN flow observations, the line of apsides of the *IBEX* orbit points largely toward the Sun, as shown in the upper panel of Figure 4. Therefore, any Earth influence, gravitational

deflection, or magnetospheric ENA background, which is addressed in Section 5.2, will be limited to observations on the descending orbit arcs. On the ascending arcs, the ISN flow reaches *IBEX* before entering the Earth's sphere of influence and its viewing is away from the magnetosphere.

In the ecliptic plane ( $x$ - $y$ ), Earth's gravitation deflects the ISN flow trajectories such that arrival exactly tangential to the Earth's orbit (ISN flow observation for exact Sun pointing of the *IBEX* spin axis) occurs at somewhat larger ecliptic

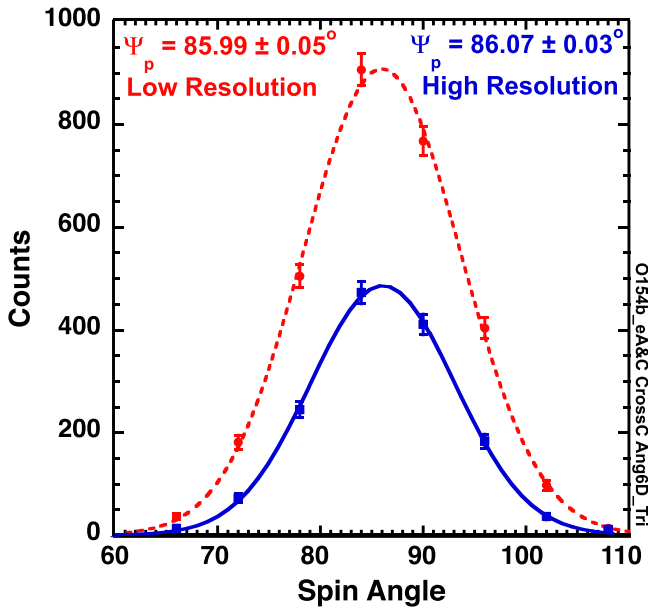


**Figure 2.** Comparison of angular He distributions for *IBEX* orbit 154b, shown in the *IBEX* spin angle, as taken solely with the high angular resolution section of *IBEX*-Lo (blue) and with the entire *IBEX*-Lo aperture (red), along with statistical error bars and fits to a Gaussian distribution. The resulting peak positions and statistical uncertainties are shown at the top.

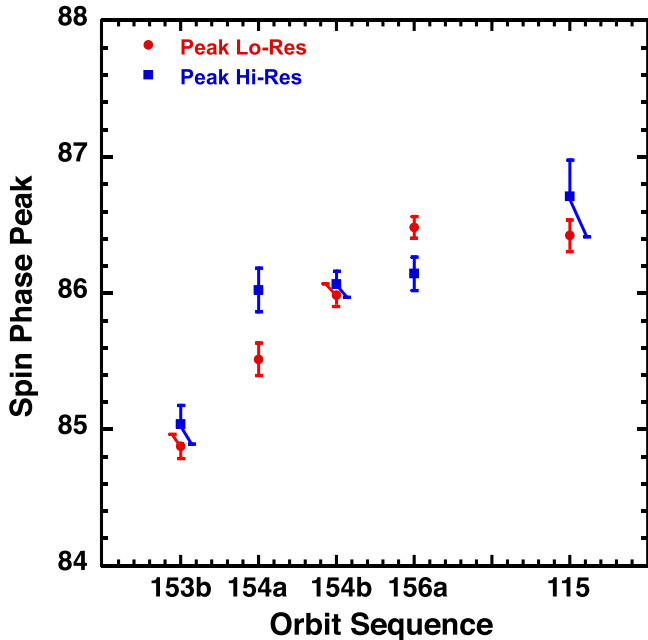


**Figure 3.** Peak locations and their statistical uncertainties are compiled for all high- and low-resolution cross-calibration periods taken in 2011 and 2012 (high-resolution section in blue and the full *IBEX*-Lo aperture in red).

longitude than without the Earth’s influence. In the plane perpendicular to the Earth–Sun line ( $y$ – $z$ ), the ISN bulk flow arrives at *IBEX* during descending arcs after passing north of the Earth–Sun line, as depicted in the bottom panel of Figure 4. Here, the gravitational influence deflects the flow so that a slightly larger negative flow latitude would be observed. Also, part of the observed distribution passes south of the Earth–Sun line, which could result in a slightly focused and widened distribution. Kucharek et al. (2015) find a maximum deflection angle of  $0^{\circ}08$  for the minimum altitude of *IBEX* operations

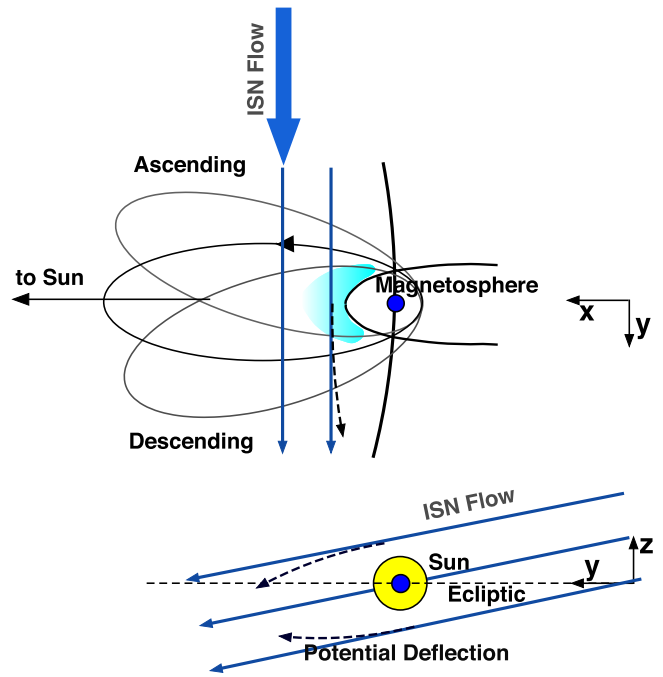


**Figure 4.** Schematic view of the potential Earth influence on the ISN flow in the ecliptic plane ( $x$ – $y$ , top) and in the plane perpendicular to the Earth–Sun line ( $y$ – $z$ , bottom) along with *IBEX* orbits and indications of their ascending and descending arcs (McComas et al. 2011) during the spring ISN flow season. Any influence due to gravitational deflection or magnetosphere-related background is limited to the descending orbit arcs. Gravitational deflection, if important, would occur away from the Sun in the  $x$ – $y$  plane and will mostly be in the negative  $z$  direction in the  $y$ – $z$  plane. Some focusing might also occur in this plane.

( $15 R_E$ ), which must be split into the components in the two planes. In addition, *IBEX* spends most of the time near the apogee of its orbit. The resulting deflection values are much smaller than both the statistical uncertainty of the bulk flow longitude, about  $0^{\circ}3$  (Möbius et al. 2012), and the combined *IBEX*-Lo pointing accuracy at a latitude of  $\pm 0^{\circ}18$ , and thus can be neglected.

#### 4. INTERSTELLAR FLOW PARAMETER ANALYSIS METHODS AND RELATED SYSTEMATIC UNCERTAINTIES

*IBEX* accumulates a complete ISN flow image over several months each spring when the Earth is moving into the flow. Thus, it scans different parts of the full distribution from different ecliptic longitude positions. In contrast, *Ulysses* GAS obtains multiple images while the spacecraft passes through each of its three perihelia from north to south. While *IBEX* provides far superior signal-to-noise and background ratios in its ISN observations, *Ulysses* has the advantage of ISN image viewing locations spread over a range of ecliptic latitudes (Bzowski et al. 2014; Wood et al. 2015b). *IBEX* observations from a limited range of locations along the Earth’s orbit require attention to various systematic effects, including the influence of the Warm Breeze, which *IBEX* discovered (Kubiak et al. 2014). We discuss the latter in more detail in Sections 5 and 6. In Sections 4.1, we briefly summarize the four different ISN flow models, followed in Section 4.2 by the three-step method that has been used by Möbius et al. (2012), Leonard et al. (2015), and Schwadron et al. (2015) to obtain the ISN flow parameters in a manner complementary to Bzowski et al.

(2012, 2015). We then use this method to assess the model accuracy in Section 4.3. In Section 4.4, we assess the systematic uncertainties of this analysis, how they are mitigated by the *IBEX* spin-axis pointing strategy, and the influence of statistical fluctuations.

#### 4.1. ISN Flow Models

For the *IBEX* ISN flow analysis, we have developed four complementary models.

1. The numerical Warsaw Test Particle Model (nWTPM) computes the ISN trajectories numerically from the observer to the boundary of the heliosphere at 150 AU where the distribution currently conforms to a convected Maxwellian (Bzowski et al. 2012; Kubiak et al. 2014). Alternative distributions have been implemented in the Warm Breeze study and in Sokół et al. (2015a), but are not considered here. At the exact *IBEX* position along the Earth’s orbit, the distributions are integrated over energy, sensor FOV, spin phase bins, and selected observation intervals. The numerical implementation allows the inclusion of spatial and temporal dependencies for the ionization rates, radiation pressure, and the time history of the spacecraft motion as needed. Although this approach is computationally intensive and challenging to use for parameter optimization, it has been successfully applied to *IBEX* (Bzowski et al. 2012, 2015; Kubiak et al. 2014; McComas et al. 2015a) and *Ulysses* (Bzowski et al. 2014) ISN flow observations. The companion paper by Sokół et al. (2015b) describes refinements introduced into the model for the current analysis.
2. The analytic Warsaw Test Particle Model (aWTPM) traces the ISN trajectories to 150 AU using analytic expressions for the motion in a static combination gravitation and radiation pressure (as appropriate). It also uses an analytic description of ionization losses that vary as  $1/r^2$  with distance from the Sun. A detailed description of this model and a comparison between the nWTPM and aWTPM are presented in Sokół et al. (2015b).
3. The analytic EXPansion Model (aEXPM; Lee et al. 2012, 2015) computes the ISN trajectories using analytic expressions for the motion in a static gravitational and radiation pressure field. Using Liouville’s Theorem the model calculates the ISN heliospheric distribution function assuming a convected Maxwellian at infinity. Integrating atom intensity over energy and a Gaussian response in solid angle about the *IBEX*-Lo pointing direction, the aEXPM uses an expansion scheme about the peak of the distribution to calculate analytical expressions for the ISN count rate peak in longitude, and its peak and width in latitude as functions of longitude. The model includes aberrations due to spacecraft motion, average ionization rates, and *IBEX* spin-axis tilt.
4. The analytic Full INtegration Model (aFINM; Schwadron et al. 2013, 2015) also computes the ISN trajectories using analytic expressions for the motion in a static gravitational and radiation pressure field. Currently, a convected Maxwellian at infinity is assumed but alternate distributions can be implemented. The observed distributions are computed by integration over energy, collimator FOV, the respective spin phase sector, and over observer

longitude according to the integration time. The collimator integration starts from the center, adapting the accuracy of the step size to optimize precision and computational performance.

#### 4.2. Complementary Analysis Methods

Starting from early analyses (Bzowski et al. 2012; Möbius et al. 2012), two models (nWTPM and aEXPM) have been used in conjunction with two distinct complementary methods of best-fit ISN flow parameter determination. Bzowski et al. (2012) determined the ISN flow parameters through a global  $\chi^2$  minimization of the nWTPM to the observed flux distributions, and Möbius et al. (2012) determined them in three consecutive steps using the aEXPM, as described below in detail. The two new models, aFINM and aWTPM, can, in principle, be employed using both of these methods. In the following, we will compare the results from the different models, which provide simulated data for an identical ISN parameter set. These are then evaluated with aEXPM. In particular, we (1) show that all four models lead to comparable results within small uncertainties, (2) evaluate several identifiable systematic uncertainties in our observations, and (3) identify the sensitivities of the two analysis methods which may have led to systematic deviations in our results. The paper by Swaczyna et al. (2015) addresses additional sensitivities of the global  $\chi^2$  minimization to uncertainties in the observations and data transfer.

As discussed in Möbius et al. (2012) and Lee et al. (2012), the determination of the ISN flow vector in either of the two methods is strongly dependent on the observation of the flux maximum (ISN bulk flow at 1 AU) perpendicular to the Earth–Sun line with the Sun-pointing *IBEX* spin axis. The ecliptic longitude  $\lambda_{\text{Peak}}$  of the ISN bulk flow perihelion at 1 AU and the ISN flow speed  $V_{\text{ISN}\infty}$  and longitude  $\lambda_{\text{ISN}\infty}$  at infinity are uniquely connected via the trajectory equation for the true anomaly  $\theta_\infty$ :

$$V_{\text{ISN}\infty} = \sqrt{\frac{GM_s}{r_E} \cdot \left( \frac{-1}{\cos(\theta_\infty)} - 1 \right)}$$

and  $\theta_\infty = \lambda_{\text{ISN}\infty} + 180^\circ - \lambda_{\text{Peak}}$ . (4.1)

The location of the flow maximum  $\lambda_{\text{Peak}}$  is determined independently using the same assumptions on ambient conditions for the two complementary analysis methods. Bzowski et al. (2012) employ a global  $\chi^2$ -minimization for all ISN parameters simultaneously to the complete observed ISN flow distribution and deduce  $\lambda_{\text{Peak}}$  as one of their results. Möbius et al. (2012) determine  $\lambda_{\text{Peak}}$  as the first step in their analysis directly from the observed fluxes and arrive at the same value within the  $\pm 0.7^\circ$  uncertainty. According to Equation (4.1),  $\lambda_{\text{Peak}}$  constrains the functional relationship  $V_{\text{ISN}\infty}(\lambda_{\text{ISN}\infty})$  to within  $\leq \pm 0.7^\circ$  in  $\lambda_{\text{ISN}\infty}$  and  $\leq \pm 0.5 \text{ km s}^{-1}$  in  $V_{\text{ISN}\infty}$ . However, a large range of  $V_{\text{ISN}\infty}(\lambda_{\text{ISN}\infty})$  combinations satisfies the observed ISN flow maximum at 1 AU. This is the allowable range of values along the ISN parameter tube in  $V_{\text{ISN}\infty}$ ,  $\beta_{\text{ISN}\infty}$  and  $T_{\text{ISN}\infty}(\lambda_{\text{ISN}\infty})$  (McComas et al. 2012). To determine the optimum set of individual parameters, the two methods diverge. Möbius et al. (2012) determine the ISN flow parameters in two further consecutive steps. It is instructive to

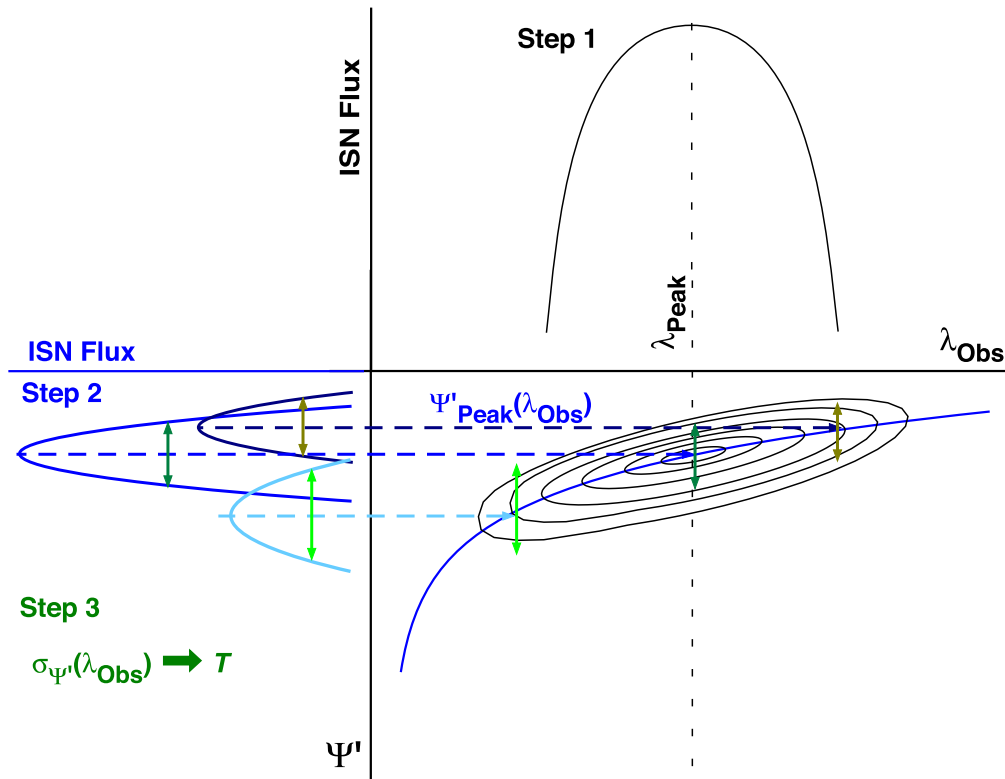


**Figure 5.** Schematic representation of the ISN flow distribution observed by *IBEX* in Earth’s orbit. Upper right: spin-integrated flux as a function of observer longitude  $\lambda_{\text{Obs}}$ . Lower left: spin phase ( $\psi'$ ) distributions. Lower right: flux isocontours in  $\lambda_{\text{Obs}}$  and  $\psi'$ . Three consecutive steps to obtain the ISN flow vector and temperature using the aEXPM (Lee et al. 2012, 2015) are indicated. The analysis starts with the peak location in observer longitude  $\lambda_{\text{Obs}}$ , followed by the peak in latitude  $\psi'$  to determine the flow vector, and concludes with the width  $\sigma$  in latitude  $\psi'$  to get the temperature.

follow this three-step method, as illustrated in Figure 5, to see in which way different statistical and systematic observational uncertainties influence the accuracy of the results.

In the lower right quadrant, Figure 5 shows schematically the ISN flow distribution as observed in the *IBEX* reference frame in latitude  $\Psi'$  (or spin phase) and ecliptic longitude  $\lambda_{\text{Obs}}$  (over consecutive orbits) as seen in *IBEX* sky maps. Using solely the spin phase-integrated ISN flux as a function of longitude, the location of the flux maximum  $\lambda_{\text{peak}}$  for the observed ISN flow distribution (or the longitude of the bulk flow) is determined. Concentrating on the bulk flow, very good fits with small fit errors are achieved because the signal/background ratio of the ISN flow peak reaches up to  $\approx 1000$ . However, it is important to include systematic effects that can shift the peak location. As a particle sensor, *IBEX*-Lo observes the flux, whereas the ISN bulk flow represents a peak in phase space density whose location is required for the analysis. The related transformation is performed in the model. The ionization losses, which depend on observer longitude, shift the observed peak to larger longitudes. Because the survival probability of He is high, a 20% uncertainty in ionization, which is an overestimate (Bzowski et al. 2015), would translate into an additional uncertainty of the peak location of only  $\Delta\lambda_{\text{peak}} = 0^\circ.1$ . The small throughput corrections applied to the ISN flow data as described by Swaczyna et al. (2015) have only a very small effect because the integral count rate in spin phase between  $\pm 3\sigma$  of the peak is used for the bulk flow analysis (Möbius et al. 2012). The absolute pointing uncertainty of  $\Delta\lambda = \pm 0^\circ.1$ , as discussed in Section 3.2, only contributes minimally to the overall error

budget. Finally, the result is appropriately corrected for the *IBEX* spacecraft motion as an aberration of the ISN flow in angle as described in Möbius et al. (2012).

In the second step, the variation of the peak location in latitude  $\Psi'_{\text{Peak}}$  as a function of  $\lambda_{\text{Obs}}$  is used to determine the ISN flow longitude  $\lambda_{\text{ISN}\infty}$  and latitude  $\beta_{\text{ISN}\infty}$  at infinity (lower left quadrant in Figure 5). Thus, the peak of the flow distribution in latitude in each orbit of the ISN observation season is used for the flow vector determination, which limits the sensitivity of the results to features in the ISN flow that contribute significantly to the peak location. This restriction makes the analysis less sensitive to background and tails of the distribution. The method effectively finds the peak location as opposed to the centroid of the full distribution. The peak location is still subject to the sensor pointing uncertainty, for which we found  $\Delta\psi' = \pm 0^\circ.18$  in this direction. Further sensitivities of the method will be evaluated in Section 4.4.

In a third and final step, the temperature is determined using the width of the ISN flow distribution as a function of the observer longitude. The  $\sigma'_{\psi'}$  width of a Gaussian distribution is determined in a  $\chi^2$  fit to the observed angular distributions, which includes convolution over the collimator FOV. Concentrating on  $\sigma'_{\psi'}$  makes the analysis less sensitive to background and low intensity tails. Any non-uniform background or foreground distributions that are wider or narrower than the ISN flow distribution and are roughly co-located in the sky may still alter the deduced width. Such potential systematic effects are addressed in Section 5.2.

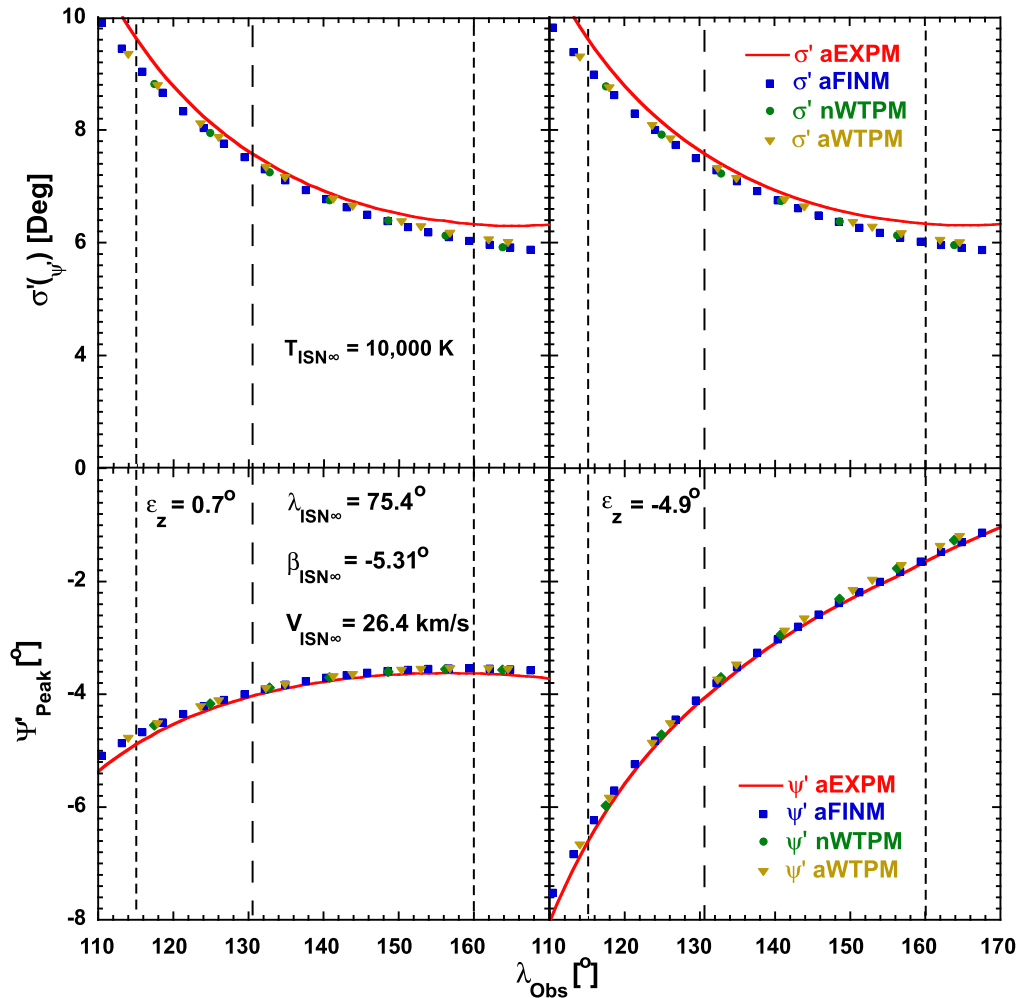


**Figure 6.** Peak location  $\psi'_{\text{Peak}}$  (bottom) and width  $\sigma'_{\psi}$  (top) in latitude as a function of observer longitude  $\lambda_{\text{Obs}}$  simulated with all four models for  $\varepsilon_z = 0.7^\circ$  (left) and  $\varepsilon_z = -4.9^\circ$  (right). The long dashed lines indicate the ISN bulk flow longitude ( $130.6^\circ$ ) and the short dashed lines the range chosen for the data analysis ( $\lambda_{\text{Obs}} = 115^\circ\text{--}160^\circ$ ).

### 4.3. Comparison of the ISN Flow Models

To discuss the systematic effects involved with the analysis of the ISN flow observations, we begin with a direct comparison of the four ISN flow models. We directly compare the peak location  $\psi'_{\text{Peak}}$  and width  $\sigma'_{\psi}$  as a function of observer longitude as obtained from each of the models for the same ISN flow parameters but various *IBEX* spin-axis orientations out of the ecliptic  $\varepsilon_z$ . We treat the output from the nWTPM, aWTPM, and aFINM simulations, which provide angular flux distributions in  $6^\circ$  sectors for specified accumulation times (and thus observer longitude ranges) as simulated data that go into our three-step method. A direct comparison of the bulk flow longitude obtained with nWTPM and aEXPM was performed by Möbius et al. (2012) and found to agree very closely. This agreement led to very similar ISN parameter tubes with the global  $\chi^2$  minimization (Bzowski et al. 2012) and the three-step method (Möbius et al. 2012), which was consolidated in McComas et al. (2012). Here, we concentrate on steps two and three.

In a first analysis step of *IBEX* observations and simulated data,  $\psi'_{\text{Peak}}$  and  $\sigma'_{\psi}$  are obtained through a  $\chi^2$  fit to a Gaussian distribution that includes the sensor FOV, similar to Möbius et al. (2012) and Leonard et al. (2015). Performing this task on

simulated data from the aFINM provides a sensitive test of whether a fit to a Gaussian distribution at 1 AU, after the original Maxwellian distribution is distorted by the Sun’s gravitational potential, returns the actual peak location or only a proxy with a substantial uncertainty. Because aFINM starts the integration over the angular distribution at the observer location from the peak to optimize computational performance (Schwadron et al. 2015), this model returns the actual peak latitude at 1 AU. We find that the fit result and the actual peak location agree to better than  $0.01^\circ$ . A noticeable, but very small, difference starts to appear for  $\lambda_{\text{Obs}} < 110^\circ$ , i.e., outside the observer longitude range used for the analysis. This result validates that a Gaussian fit to the observed angular distributions indeed returns the correct peak location and width for further analysis, as long as the original distribution can be modeled as a single Maxwellian.

Figure 6 shows the peak location  $\psi'_{\text{Peak}}$  and width  $\sigma'_{\psi}$  in latitude of the ISN flow distribution seen by *IBEX* as a function of  $\lambda_{\text{Obs}}$  for all four models. We show the results for two different spin-axis pointing directions out of the ecliptic plane:  $\varepsilon_z = 0.7^\circ$  (used 2009 through 2011) and  $\varepsilon_z = -4.9^\circ$  (used in 2014). All models use identical ISN flow parameters ( $\lambda_{\text{ISN}\infty} = 75.4^\circ$ ,  $\beta_{\text{ISN}\infty} = -5.31^\circ$ ,  $V_{\text{ISN}\infty} = 26.4 \text{ km s}^{-1}$ , and  $T_{\text{ISN}\infty} = 10,000 \text{ K}$ ) at the ends of the trajectories (infinity for

aFINM and aEXPM, and 150 AU for nWTPM and aWTPM). There are only very small differences ( $\leq 0^\circ 05$ ) between nWTPM/aWTPM and aFINM in peak location and width. The aEXPM also reproduces the peak position within  $< 0^\circ 1$ , except for  $\lambda_{\text{Obs}} < 115^\circ$ . The width is within  $< 0^\circ 15$  of the other three models exactly at the bulk flow location, but deviates visibly toward larger and smaller longitudes.

The small deviations of aEXPM relative to the other models may be attributed to the expansions used in this model. Terms higher than second order are omitted (Lee et al. 2015). This truncation leads to a result that, for example, contains the peak locations according to phase space density, while the observations are taken in flux. The direction of the small deviations is consistent with the expected difference. However, since other third-order terms are omitted, no attempt is made to include any higher-order terms. As can be seen from the bottom panels, the peak location in latitude is reproduced accurately enough so that aEXPM can be used to determine the ISN flow longitude  $\lambda_{\text{ISN}\infty}$  and latitude  $\beta_{\text{ISN}\infty}$  from observations of this peak. Also, the determination of the He temperature from the widths of the distributions in orbits 16 and 64, i.e., the ones closest to the ISN bulk flow observation in Möbius et al. (2012), carried only a small error. With aEXPM resulting in an approximately  $0^\circ 15$  wider distribution for an observed  $\sigma'_\psi \approx 7^\circ 5$ , this difference led to a 4% lower temperature than would be obtained with the other models. To accurately include the full range of ISN flow data, the other models should be used.

#### 4.4. Sensitivity of the Analysis to Various Uncertainties

We are now in a position to test the robustness of fit results using the three-step method for the ISN flow vector between the models as well as their sensitivity to uncertainties in the *IBEX* observations and intrinsic to this method. We use the resulting peak locations  $\psi'_{\text{Peak}}$  from fits to a Gaussian along with the fit uncertainty. To obtain results that are comparable with what to expect from the observations, we scale the fit uncertainties of the simulated data so that the smallest uncertainties for the ISN flow peak location do not drop below  $0^\circ 07$  as typically found for the observations. As in Möbius et al. (2012) and Leonard et al. (2015), we perform a  $\chi^2$ -minimization of  $\psi'_{\text{Peak}}(\lambda_{\text{Obs}})$  of the aEXPM to the other model results. In aEXPM, we include the collimator integration to obtain the peak locations (Lee et al. 2015). As can be seen in Figure 6, this modification to the model has eliminated the dependence of the fit results on the spin-axis orientation out of the ecliptic  $\varepsilon_z$ , which was reported by Leonard et al. (2015).

Table 1 shows the resulting  $\lambda_{\text{ISN}\infty}$  and  $\beta_{\text{ISN}\infty}$  values along with the reduced  $\chi^2$  and  $1\sigma$  fit uncertainties for the three different spin-axis orientations ( $\varepsilon_z = 0^\circ 7, 0^\circ$ , and  $4^\circ 9$ ) that have been used thus far. Shown in row one are simulation results from nWTPM, two from aWTPM, and four from aFINM (in bold face for further comparison), all for the same model input at the end of the atom trajectories and with an ionization rate that represents the average for the 2009 observations. A fit with the aEXPM now returns an ISN flow vector for all spin-axis orientations that is close to the input parameters in  $\lambda_{\text{ISN}\infty}$  and  $\beta_{\text{ISN}\infty}$ , although with some noticeable variations. The values are very close for the comparison with aFINM with the largest difference being  $0^\circ 7$  in  $\lambda_{\text{ISN}\infty}$  for  $\varepsilon_z = -4^\circ 9$ . The fit results to nWTPM and aWTPM are almost identical, but consistently arrive at larger  $\lambda_{\text{ISN}\infty}$  values by about  $0^\circ 8, 1^\circ$ , and  $1^\circ 5$ . This result is interesting because  $0^\circ 7$  of this

shift can be attributed to the fact that both models use 150 AU tracking distance for the trajectories. An ISN flow longitude of  $75^\circ 4$  at 150 AU, as used for these simulations, is equivalent to  $76^\circ 1$  at infinity. In other words, the nWTPM and aWTPM simulations were carried out with  $\lambda_{\text{ISN}\infty} = 76^\circ 1$  at infinity. The reduced  $\chi^2$  values are all much smaller than 1, which would normally be attributed to data point uncertainties that are much too small. However, in our comparison, we use simulated data points with no intrinsic variation and model curves that are well represented by either model, which largely explains the small values. We will come back to this point with an attempt to introduce statistical variations at the end of this section.

The fit results in row three have been obtained with aWTPM simulations with the ionization rate set to 0. The resulting values for  $\lambda_{\text{ISN}\infty}$  and  $\beta_{\text{ISN}\infty}$  are almost identical to the comparable simulations with ionization in row two. We can conclude that the effect of ionization on the ISN flow direction results in the three-step method is negligible. It should be noted, however, that knowledge of this is needed for the determination of the bulk flow longitude  $\lambda_{\text{Peak}}$ .

The next two sets, simulated with aFINM, show what happens when the bulk flow longitude is either increased or decreased by  $0^\circ 7$ , equivalent to an overall uncertainty in  $\lambda_{\text{Peak}}$  as reported by Möbius et al. (2012). For  $\varepsilon_z = 0^\circ$  and  $\varepsilon_z = 0^\circ 7$ , the flow longitude results are within  $0^\circ 1$  of the original results, and for  $\varepsilon_z = -4^\circ 9$  they are still within  $0^\circ 3$ . This result means that the bulk flow peak location  $\lambda_{\text{Peak}}$ , which determines the four-dimensional (4D) ISN parameter tube, is almost independent of the flow longitude and latitude result, or the second step of the method. This interesting result can be readily understood from the observation geometry for  $\varepsilon_z = 0^\circ$ . It also follows from this result that the small pointing uncertainty of  $\pm 0^\circ 1$  in longitude has a negligible effect on the ISN flow vector.

Finally, we study how the combined absolute pointing uncertainty in latitude from Section 3.3 affects the resulting ISN flow vector. To test this effect, we have added  $+0^\circ 18$  or  $-0^\circ 18$  to the simulated peak latitudes. Comparing the last two sets with the first comparison set, the flow latitude  $\beta_{\text{ISN}\infty}$  changes by  $\pm 0^\circ 28$ , i.e., the uncertainty modified by the frame transformation, as expected. The resulting  $\lambda_{\text{ISN}\infty}$  values change by about  $\pm 1^\circ$  for  $\varepsilon_z = 0^\circ$  and  $0^\circ 7$ , but only by about  $\pm 0^\circ 7$ , or half the value, for  $\varepsilon_z = -4^\circ 9$ . Apparently, the spin-axis pointing out of the ecliptic plane, in this case with a negative tilt, or slightly non-orthogonal scanning of the flow peak makes the ISN flow vector determination more robust against the absolute pointing uncertainty.

To also evaluate the effect of purely statistical uncertainties on the analysis, we have taken simulated angular distributions and added noise to each data point with a random number generator, assuming a Poisson distribution with the simulation result as the expectation value. For our experiment, we have calculated the expected number of counts for a total accumulation time of 32 *IBEX*-Lo instrument cycles in the special ISN mode (16,384 spins or about 65 hr), which corresponds to reasonably good coverage over one orbit arc. We repeat the comparison of the aWTPM simulation with and without ionization for  $\varepsilon_z = 0^\circ$ . Figure 7 shows the original simulated peak latitudes and, for the first trial with each simulated set, the randomized peaks with  $1\sigma$  uncertainties, along with the  $\chi^2$  fit to aEXPM, in the left panel without ionization and in the center panel with ionization. The original simulated peak locations are shown in direct comparison of the two cases in the right panel. Although the original peak

**Table 1**  
ISN Flow Vector  $\chi^2$  Fit Results for Simulated Distributions with the Different Models

$\varepsilon_z$	0°:7		0°:0		-4°:9	
$\lambda_{\text{Peak}} = 310:6$	Results	Red $\chi^2$	Results	Red $\chi^2$	Results	Red $\chi^2$
nWTPM Ionization						
$\lambda_{\text{ISN}\infty}$	<b>76°:20 ± 0°:21</b>	<b>0.09</b>	<b>76°:57 ± 0°:67</b>	<b>0.12</b>	<b>77°:06 ± 0°:23</b>	<b>0.65</b>
$\beta_{\text{ISN}\infty}$	<b>-5°:23 ± 0°:01</b>	...	<b>-5°:26 ± 0°:03</b>	...	<b>-5°:68 ± 0°:02</b>	...
aWTPM Ionization						
$\lambda_{\text{ISN}\infty}$	<b>76°:25 ± 0°:22</b>	<b>0.10</b>	<b>76°:48 ± 0°:63</b>	<b>0.11</b>	<b>77°:06 ± 0°:21</b>	<b>0.57</b>
$\beta_{\text{ISN}\infty}$	<b>-5°:24 ± 0°:02</b>	...	<b>-5°:27 ± 0°:03</b>	...	<b>-5°:47 ± 0°:01</b>	...
aWTPM No Ionization						
$\lambda_{\text{ISN}\infty}$	76°:27 ± 0°:23	0.10	76°:53 ± 0°:68	0.12	77°:06 ± 0°:22	0.56
$\beta_{\text{ISN}\infty}$	-5°:23 ± 0°:02	...	-5°:26 ± 0°:03	...	-5°:48 ± 0°:02	...
aFINM Ionization						
$\lambda_{\text{ISN}\infty}$	<b>75°:65 ± 0°:15</b>	<b>0.05</b>	<b>75°:49 ± 0°:39</b>	<b>0.04</b>	<b>74°:69 ± 0°:05</b>	<b>0.03</b>
$\beta_{\text{ISN}\infty}$	<b>-5°:18 ± 0°:01</b>	...	<b>-5°:21 ± 0°:02</b>	...	<b>-5°:31 ± 0°:01</b>	...
$\lambda_{\text{Peak}} + 0°:7$						
$\lambda_{\text{ISN}\infty}$	75°:70 ± 0°:15	0.05	75°:53 ± 0°:38	0.04	74°:67 ± 0°:04	0.02
$\beta_{\text{ISN}\infty}$	-5°:18 ± 0°:01	...	-5°:20 ± 0°:02	...	-5°:24 ± 0°:01	...
$\lambda_{\text{Peak}} - 0°:7$						
$\lambda_{\text{ISN}\infty}$	75°:60 ± 0°:15	0.05	75°:39 ± 0°:36	0.04	74°:41 ± 0°:02	0.01
$\beta_{\text{ISN}\infty}$	-5°:19 ± 0°:01	...	-5°:22 ± 0°:02	...	-5°:40 ± 0°:01	...
$\psi'_{\text{Peak}} + 0°:18$						
$\lambda_{\text{ISN}\infty}$	76°:64 ± 0°:13	0.03	76°:40 ± 0°:34	0.03	75°:27 ± 0°:05	0.05
$\beta_{\text{ISN}\infty}$	-4°:90 ± 0°:01	...	-4°:93 ± 0°:02	...	-5°:04 ± 0°:01	...
$\psi'_{\text{Peak}} - 0°:18$						
$\lambda_{\text{ISN}\infty}$	74°:76 ± 0°:17	0.07	74°:66 ± 0°:43	0.06	73°:79 ± 0°:02	0.01
$\beta_{\text{ISN}\infty}$	-5°:46 ± 0°:01	...	-5°:49 ± 0°:02	...	-5°:60 ± 0°:01	...

**Note.** The rows with bold values provide a direct comparison between the three ISN flows models nWTPM, aWTPM, and aFINM.

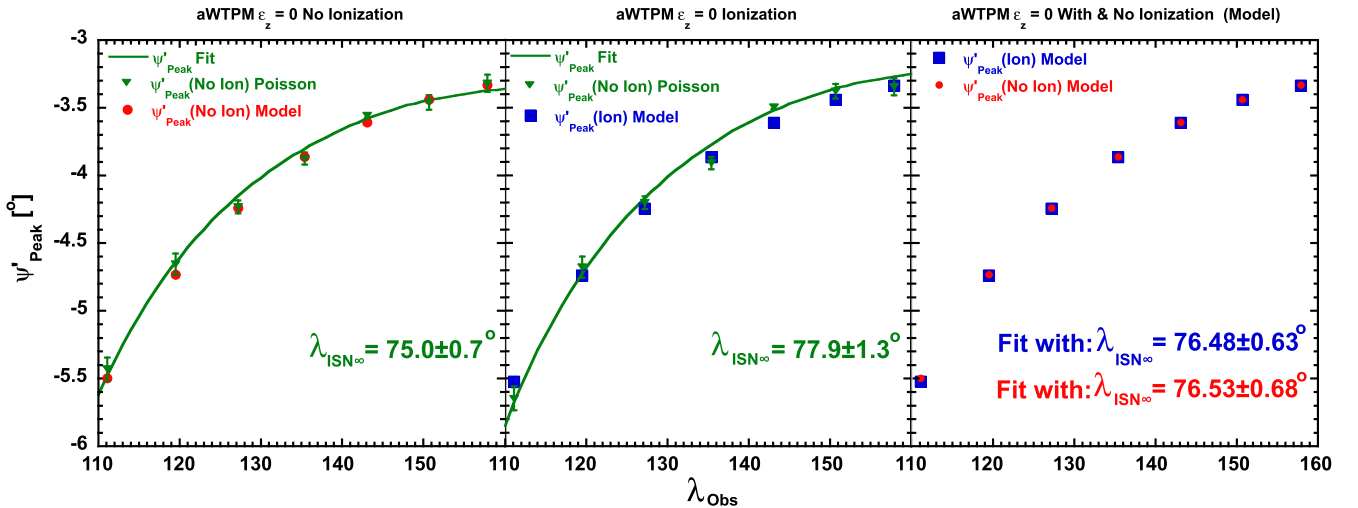


**Figure 7.** Simulated ISN peak latitudes at exact Sun pointing for orbits 13–19 (squares) without (left) and with ionization (center), together with Poisson randomized latitudes and  $1\sigma$  uncertainties from the Gaussian fit to the simulated distributions and with fit lines to the aEXPM after  $\chi^2$  minimization. The original simulated peak locations for the two cases are shown in direct comparison on the right.

latitudes are almost indistinguishable and the  $\chi^2$  fits to these points return almost identical results, as already shown in Table 1, these first trials with randomized distributions lead to starkly different ISN flow vector results, by about  $3^\circ$  in  $\lambda_{\text{ISN}\infty}$ . This

difference is mostly due to the leftmost simulated data point, which deviates from the original value by slightly more than  $1\sigma$  to a less negative latitude in the left panel and to a more negative latitude in the center panel. Apparently, one single data point, as

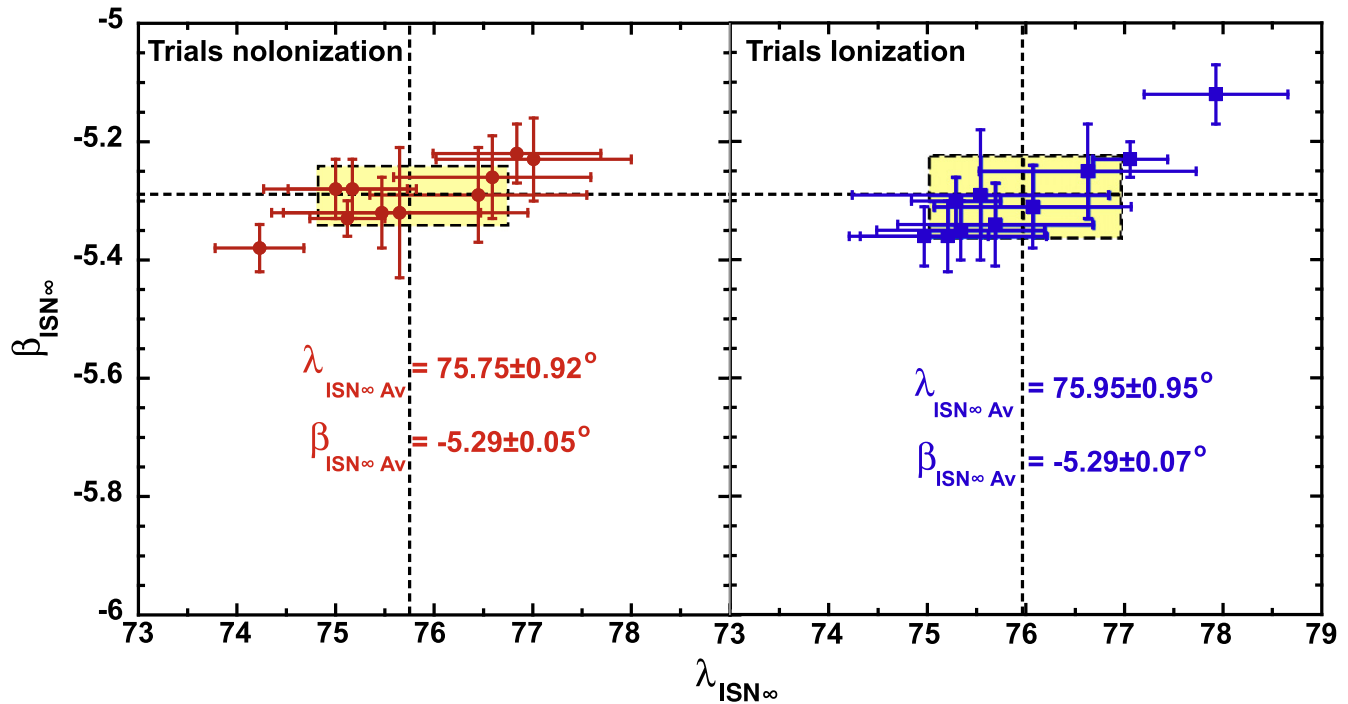


**Figure 8.**  $\lambda_{\text{ISN}\infty}$  and  $\beta_{\text{ISN}\infty}$  values from  $\chi^2$  fits to the peak latitudes from the aWTPM simulation with  $\varepsilon_z = 0^\circ$ , both without (left) and with (right) ionization along with  $1\sigma$  error bars after 10 trials of Poisson randomization for each. Also shown are the average values (dashed lines) of the two ISN parameters together with the standard deviations (shaded box) of the trials.

represented by the simulated data, which deviates from the expected mean value by only slightly more than  $1\sigma$  can have a substantial effect on the derived ISN flow vector.

Subsequently, we have analyzed 10 trials total for each of the two simulated sets in the same manner. Figure 8 shows the resulting ISN parameter  $\lambda_{\text{ISN}\infty}$  and  $\beta_{\text{ISN}\infty}$  values along with  $1\sigma$  error bars without ionization on the left and with ionization on the right. The average  $\lambda_{\text{ISN}\infty}$  values for the two trial sets are within  $0.2^\circ$ , with standard deviations close to  $\pm 1^\circ$ . Also visible is the correlation between  $\lambda_{\text{ISN}\infty}$  and  $\beta_{\text{ISN}\infty}$  that is found in the observations.

This random Poisson trial result resonates with the finding by Schwadron et al. (2015), who show that flow longitudes obtained for individual years may vary with a standard deviation of  $\pm 2^\circ$ , while the results from larger multi-year selections are much more robust. The experiment with Poisson noise in simulated data shows that a large fraction of the parameter variations from year to year in the analysis of observations can simply be caused by statistical fluctuations, typically  $\pm 1^\circ$ , which likely hinges on the highly nonlinear dependence of the  $\lambda_{\text{ISN}\infty}$  results on the observed peak locations. The remainder of the  $\pm 2^\circ$  variations in the observations may be attributed to systematic effects, such as the specific distribution of available observation times and varying influence from the Warm Breeze.

Our sensitivity analysis has shown that solely using the observer longitude dependence of the ISN peak location in latitude  $\psi'_{\text{Peak}}(\lambda_{\text{Obs}})$  to deduce the ISN flow vector direction leads to a robust result as far as the influence of systematic uncertainties and differences in our models are concerned. However, even with good counting statistics for the observed angular distributions, statistical fluctuations lead to substantial variations in the results obtained from single-year data sets. Thus, the combination of multiple years is needed. As is seen

from the sensitivity analysis, a variation in the spin-axis pointing further improves the situation.

## 5. RELATION BETWEEN ISN FLOW PEAK WIDTH AND TEMPERATURE

Now we turn to the temperature determination using the width of the distributions. We will also assess how sensitive the ISN parameters are to a flow distribution that deviates from a Maxwellian distribution at infinity due to a secondary population. As introduced in Section 4.1, the observed width of the ISN flow distribution in latitude  $\sigma'_\psi$  is used in a third step to determine the ISN flow temperature. The width of the distribution  $\sigma'_\psi$  is solely a function of the ratio  $T_{\text{ISN}\infty}/V_{\text{ISN}\infty}^2$ . Because  $V_{\text{ISN}\infty}$  is linked to  $\lambda_{\text{ISN}\infty}$  through Equation (4.1),  $T_{\text{ISN}\infty}$  is obtained as a function of  $\lambda_{\text{ISN}\infty}$  within the allowable ISN parameter range (Möbius et al. 2012, 2014; Leonard et al. 2015; McComas et al. 2015a) and is then connected to the result for  $\lambda_{\text{ISN}\infty}$ . The overall uncertainty for  $T_{\text{ISN}\infty}$  also includes the allowable range in  $\lambda_{\text{ISN}\infty}$ . However, we separate the uncertainties in  $T_{\text{ISN}\infty}$  for any given  $V_{\text{ISN}\infty}$ , which is helpful in two respects. First, ISN temperatures obtained from two different spacecraft, e.g., *IBEX* and *Ulysses*, which measure the width of the flow, are comparable for common  $V_{\text{ISN}\infty}$  values, and thus uncertainties in  $\lambda_{\text{Peak}}$  and  $\lambda_{\text{ISN}\infty}$  need not be added. Second, the temperatures of two different species, i.e., He and O, can be compared for any given  $V_{\text{ISN}\infty}$  with uncertainties solely related to the observed angular width of the distributions.

### 5.1. Determination of the ISN Temperature

To determine the ISN temperature, we start from the same angular flow distributions used in Steps 1 and 2 of our method with the same criteria as before (Leonard et al. 2015). We now use the  $\sigma'_\psi$  width obtained in a fit of a Gaussian to the observed

distributions, which includes the *IBEX*-Lo FOV. Therefore, the deduced  $\sigma'_{\psi}$  corresponds to the actual width of the gas flow. Equation (5.1) shows  $\sigma_{\psi}$  in the inertial frame based on a second-order expansion of the distribution about the ISN flow peak at 1 AU (Lee et al. 2015) as a function of  $\lambda_{\text{Obs}}$ .

$$\sigma_{\psi}^2 = t \left/ \left( 2v_{\text{ISN}}^2 \left[ \frac{v_{\text{ISN}}^2(2 + v_{\text{ISN}}^2)}{(1 + v_{\text{ISN}}^2)^2} + 2 \frac{\cos \beta_{\text{ISN}\infty} (\cos \lambda_{\text{Obs}} - \cos \lambda_{\text{Peak}})}{(1 + v_{\text{ISN}}^2)} - \cos^2 \beta_{\text{ISN}\infty} (\cos \lambda_{\text{Obs}} - \cos \lambda_{\text{Peak}})^2 \right] \right) \right). \quad (5.1)$$

Here, the normalized temperature  $t = 2 k_{\text{B}} T_{\text{ISN}\infty} / (m_{\text{He}} V_{\text{E}}^2)$  is used (Lee et al. 2012, 2015), where  $V_{\text{E}}$  is the orbital speed of the Earth,  $m_{\text{He}}$  is the mass of helium, and  $k_{\text{B}}$  is the Boltzmann constant.  $v_{\text{ISN}}$  is the interstellar flow speed normalized to the orbital speed of the Earth. The width in the observer frame  $\sigma'_{\psi}$ , which is related to  $\sigma_{\psi}$  through a Galilean transformation, varies with observer longitude. This variation needs to be included when determining  $T_{\text{ISN}\infty}$  from multiple orbits during the ISN flow season. In contrast to the peak in latitude  $\Psi'_{\text{Peak}}$ , the width in Equation (5.1) is exact in the offset angle from the precise Sun pointing of the *IBEX* spin axis  $\varepsilon_{\text{E}}$  in the ecliptic and  $\varepsilon_z$  out of the ecliptic. It solely depends on the observer longitude  $\lambda_{\text{Obs}}$ .

To see how well the predicted width of the ISN flow distribution agrees between the different models, we have evaluated  $\sigma'_{\psi}(\lambda_{\text{Obs}})$  for a master parameter set  $\lambda_{\text{ISN}\infty} = 75^{\circ}4$ ,  $\beta_{\text{ISN}\infty} = -5^{\circ}31$ ,  $V_{\text{ISN}\infty} = 26.4 \text{ km s}^{-1}$ , and  $T_{\text{ISN}\infty} = 10,000 \text{ K}$ . The results for a comparison of four models, nWTPM (Sokół et al. 2015b), aEXPM (Lee et al. 2012, 2015), aFINM (Schwadron et al. 2013, 2015), and aWTPM (Sokół et al. 2015b) are shown in the upper two panels of Figure 7 for  $\varepsilon_z = 0^{\circ}$  and  $\varepsilon_z = -4^{\circ}9$ . At the ISN flow maximum  $\lambda_{\text{Obs}} = 130^{\circ}6$ , the width calculated from all four models agrees very well. aEXPM returns a width that is larger by  $0^{\circ}15$  than the other three models, which agree within  $<0^{\circ}1$ . Toward larger and smaller observer longitudes,  $\sigma'_{\psi}$  from aEXPM deviates noticeably from the other models (up to  $0^{\circ}5$  for  $115^{\circ}$ – $160^{\circ}$  used for data analysis), which translates into temperature differences of 4%–16% that are too large to be ignored.

Because the other three models agree with one another, here we use aFINM (Schwadron et al. 2013, 2015). We use simulated aFINM data for an ISN parameter set with  $T_{\text{ISN}\infty} = 9000 \text{ K}$ , i.e., close to the temperatures determined from *IBEX* data, and then scale  $\sigma'_{\psi}$  as  $\sqrt{T_{\text{ISN}\infty}/9000 \text{ K}}$  in our comparison with the observations, making use of the fact that the width  $\sigma'_{\psi}$  only depends on the temperature as a scaling factor (Equation (5.1)). We have tested this scaling for  $T_{\text{ISN}\infty} = 7000$ – $10,000 \text{ K}$  and  $115^{\circ} < \lambda_{\text{Obs}} < 140^{\circ}$  against simulated aFINM values and find that any deviations are smaller than  $-0.4\%$  at  $115^{\circ}$  and  $+0.9\%$  at  $160^{\circ}$ .

Figure 9 shows the ISN flow width  $\sigma'_{\psi}$  for  $115^{\circ} \leq \lambda_{\text{Obs}} \leq 160^{\circ}$  and the entire ISN data set from 2009 through 2014. Shown are  $\chi^2$  fits to all data (solid line) and separately to the longitude ranges  $<140^{\circ}$  (long dashed line) and  $>140^{\circ}$  (short dashed line), along with the fit values and the  $1\sigma$  statistical uncertainties. The fit line to the entire longitude range

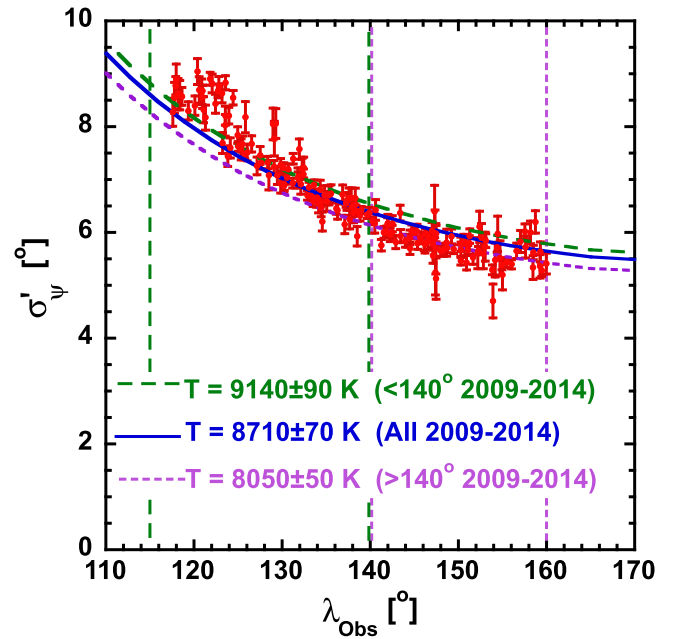


**Figure 9.** He ISN flow width and  $\chi^2$ -fit results for the 2009–2014 *IBEX* observations. Resulting values are shown for  $V_{\text{ISN}\infty} = 26.0 \text{ km s}^{-1}$  based on fits to aFINM simulations. Solid line:  $\chi^2$  fit performed for the entire range  $115^{\circ} \leq \lambda_{\text{Obs}} \leq 160^{\circ}$  as used for the He ISN Flow analysis. Short dashed line:  $\chi^2$  fit for  $\lambda_{\text{Obs}} < 140^{\circ}$ . Long dashed line:  $\chi^2$  fit to  $\lambda_{\text{Obs}} > 140^{\circ}$ . Separate  $\chi^2$  fits were performed to test how the  $T$  determination varies with  $\lambda_{\text{Obs}}$ .

appears to vary less with  $\lambda_{\text{Obs}}$  than the data, falling below the data points at smaller longitudes and above at larger longitudes. This visual interpretation is supported by the fit results to the separate ranges, which lead to a noticeably higher temperature at lower longitudes by  $>1\sigma$ . This result is consistent for all *IBEX* ISN flow seasons analyzed thus far.

Clearly, for  $V_{\text{ISN}\infty} = 26 \text{ km s}^{-1}$ , which corresponds to  $\lambda_{\text{ISN}\infty} = 76^{\circ}$ , we find He temperatures between 8000 and 9000 K, which is close to the central aFINM curve chosen for the fitting. In the following, we will discuss the systematic effects that influence the ISN temperature determination and which may, in particular, contribute to the observed trend of the resulting temperature over the chosen range in observer longitude.

## 5.2. Systematic Uncertainties in the ISN Flow Temperature Determination

Obviously, there are substantial systematic effects and, perhaps, temporal and spatial variations that are larger than the statistical uncertainties based on the  $\chi^2$  fits. Here, we first discuss the effects on the derived temperature from restrictions in the data transmission between the sensor and the CEU, followed by the effective sensor pointing and potential deflection of the ISN flow by the Earth. Then, we turn to small inhomogeneous background signals, which point to a potentially large influence from the Warm Breeze (Kubiak et al. 2014) on the inferred temperatures.

### 5.2.1. Restriction in Data Transmission

As pointed out in Möbius et al. (2012), the maximum throughput of the data transmission across the interface between *IBEX*-Lo and the CEU was suspected as a potential source that could widen the observed angular distributions for

high total count rates, above  $100 \text{ counts s}^{-1}$ . However, as discussed in Frisch et al. (2015) and Möbius et al. (2015), this effect is small because it scales with the dynamic range of the count rates as a function of the angle, while the majority of the rate contribution comes from rather homogenous background rates that are filtered out by the *IBEX*-Lo TOF system. During the 2009–2012 ISN flow seasons, the maximum effect on the derived temperature is an increase of 2.5%, for which we have corrected the 2009–2012 data used in this analysis. After 2012, *IBEX*-Lo was run in a mode that eliminates the background events at the sensor level so that they do not contribute to the data traffic. A detailed description of these effects and related corrections is given in Swaczyna et al. (2015).

### 5.2.2. Effects of Pointing Uncertainties on the Width of the Distributions

As discussed in Section 3.1, the relative pointing in latitude, or spin phase, between the high and low angular resolution *IBEX*-Lo apertures is known to within  $\pm 0^\circ.15$ . This value can be interpreted as a pointing uncertainty between the aggregate of the three low-resolution quadrants of the sensor and the high-resolution quadrant. Assuming that the three low-resolution quadrants have approximately equal sensitivities, the two quadrants oriented along the spin axis provide a symmetric response in spin phase, but the remaining low-resolution quadrant could deviate in its pointing from the collimator boresight by up to  $0^\circ.45$ . Also, the high-resolution quadrant, which contributes 8% to the total geometric factor, may deviate by up to  $0^\circ.45$  in the opposite direction. Combining the effective contributions at the level of 61.3% (2 quadrants) along the boresight, 30.7% (1 quadrant) at  $+0^\circ.45$ , and 8% (1 high-resolution quadrant) at  $-0^\circ.45$ , results in an effective FOV widening by  $0^\circ.25$  FWHM. Because this is an independent contribution to the width, the effect is equivalent to a convolution with an additional instrument profile with  $0^\circ.25$  FWHM, or  $\sigma_p = 0.11$ . For typical values of  $\sigma_{\psi'} = 6.5$  for the ISN He distribution and  $\sigma_{\psi'} = 3.2$  for O and Ne, the widening is much less than  $1/1000$ .

### 5.2.3. Deflection of the ISN Trajectories by the Earth

As discussed in Kucharek et al. (2015), even the maximum deflection of the ISN trajectories at a satellite distance of  $15 R_E$  from the Earth leads to a widening of the angular ISN flow distribution by less than  $1/1000$  for the observed widths. Therefore, the effect on the derived He and O+Ne temperatures is negligible.

### 5.2.4. Effects of Contributions from Additional Signals with Wider Angular Distribution

A uniform background lifts the total count rate of the observed angular distribution with no effect on the derived width. However, any contribution from another population with a different angular distribution can alter the derived width, and thus the resulting temperature, depending on the width and the fractional contribution to the observed distribution. Therefore, we have simulated the expected effect for a variety of conditions. The maximum effect on the observed angular width comes from an additional distribution whose peak is co-located with the distribution of interest.

The left panel of Figure 10 shows the simulated combination of an assumed angular signal distribution with  $\sigma = 7.5$  and

another distribution with  $\sigma = 15^\circ$  (background or secondary population) at 10% of the peak flux of the main distribution. The fit to the combination results in  $\sigma = 8.0$ , i.e., wider by 6.6%, which translates into a derived temperature that is 13% higher than without the additional contribution. However, the additional contribution is visible as elevated wings in the combined angular distribution, which are indeed observed in the ISN flow distribution with increased visibility toward smaller observer longitude (Bzowski et al. 2012). These wings have recently been attributed to the Warm Breeze, a secondary ISN flow component (Kubiak et al. 2014). We come back to this aspect below. In the right panel of Figure 10, the increases in  $\sigma$  and the derived temperature  $T_{\text{ISN}\infty}$  are shown as a function of the fractional contribution of a background distribution with  $\sigma = 15^\circ$ . It is obvious that an increasing fractional contribution from any wider source distribution to the primary signal (the ISN flow) leads to an increase in the temperature derived from the combined distribution. This result agrees with the apparent increase in the derived ISN He temperature as a function of observer longitude and the increasing tails in the observed ISN flow at smaller longitudes (Bzowski et al. 2012). The combination of these indicators suggests that the Warm Breeze (Kubiak et al. 2014) may be a possible explanation for the observed trend in the derived He temperature.

However, there are two possible alternative or additional explanations: contributions from Earth-related foregrounds or an ISN flow distribution that is genuinely non-Maxwellian. As far as Earth-related foregrounds, such as ENAs from the magnetosphere and/or the magnetosheath or foreshock region (Fuselier et al. 2010), are concerned, we have largely eliminated them through data selection (Möbius et al. 2012; Leonard et al. 2015). However, we conduct an additional test using the *IBEX* orbit configuration during the ISN flow observations. As shown in Figure 4, *IBEX* views the ISN flow away from the Earth during the ascending arcs, but through the region in front of the subsolar magnetopause during the lower part of the descending arcs. Therefore, we have compared the derived temperatures for all ascending and descending arcs separately during the 2012–2014 ISN flow seasons after the *IBEX* orbit change. Note that the mean observer longitudes for each separate sample may differ from each other. In fact, the temporal phasing of comparable orbit arcs have been very stable from year to year so that there is indeed a visible difference in average longitude between the ascending and descending arcs. Therefore, we have detrended the derived temperatures to reflect the values at the average observer longitude for each pair of ascending and descending arc selections according to a linear trend in the derived temperature with observer longitude, as obtained from Figure 9. The resulting temperatures for the three samples of ascending and descending arcs are compiled in Table 2, along with the  $\chi^2$ -fit errors and the average observer longitudes. The derived temperature values for the entire longitude range and for  $<140^\circ$  agree within the  $1\sigma$  fit errors, but there is a small yet visible difference that exceeds  $3\sigma$  between the ascending and descending arcs for longitudes  $>140^\circ$ . The temperature derived from the descending arcs is higher by 340 K, which could point to a small contamination by magnetospheric ENAs from the subsolar region of the magnetopause during these orbits. It is reasonable that such a small contribution appears during the later orbits, but not during earlier orbits because the ISN flow distribution decreases rapidly in intensity between  $\lambda_{\text{Obs}} = 140^\circ$

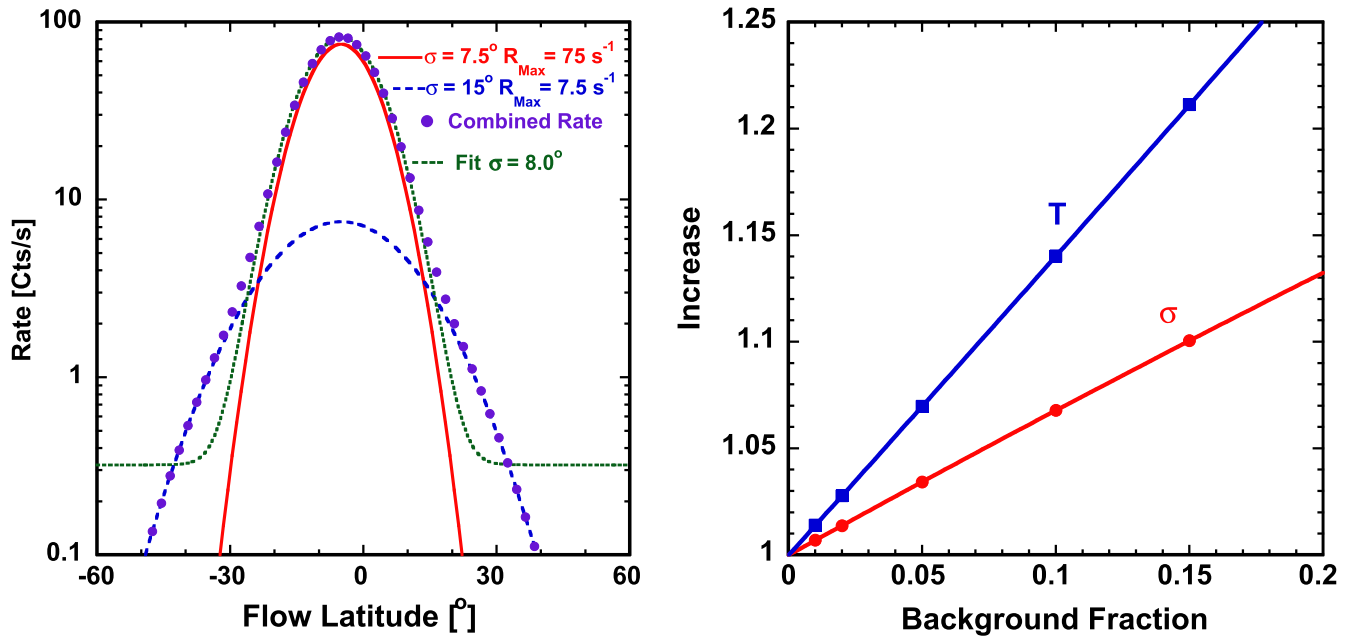


**Figure 10.** Left: simulated Gaussian distribution with  $\sigma = 7.5^\circ$  (solid), a 10% background contribution with  $\sigma = 15^\circ$  (long dashed), and a Gaussian fit to the combined distribution (short dashed). Right: expected increase of the resulting  $\sigma$  width and derived temperature  $T_{\text{ISN}\infty}$  as a function of the background fraction with the parameters used in the left panel.

**Table 2**

Temperature Fits Separated for Ascending and Descending Orbit Arcs

	$\lambda_{\text{Obs}} < 140^\circ$	$\lambda_{\text{Obs}} > 140^\circ$	$115^\circ < \lambda_{\text{Obs}} < 160^\circ$
$\lambda_{\text{Obs\_Mean}}$	128:7	149:7	137:5
$T_{\text{Ascending}}$	9140 $\pm$ 170 K	7890 $\pm$ 80 K	8650 $\pm$ 100 K
$T_{\text{Descending}}$	8970 $\pm$ 100 K	8230 $\pm$ 100 K	8610 $\pm$ 90 K

and  $160^\circ$ , while the peak of the ISN flow occurs at  $\lambda_{\text{Obs}} \approx 130^\circ$  where the signal-to-noise/background ratio reaches 1000. The difference in these late orbit arcs with lower signal-to-background ratio is only about 4% in the derived temperature. Thus, the suspected effect from combined ascending and descending arcs is at most 2%, and any such contamination must indeed be negligible for the full range and smaller observer longitudes.

Finally, we ask whether the pristine ISN flow distribution is possibly non-Maxwellian and may be better represented by a  $\kappa$ -distribution. If true, then when fitting the distribution with a Maxwellian, the derived temperature will be lower than for the equivalent  $\kappa$ -distribution. Attempts to account for such deviations from a thermal distribution are ongoing (Kubiak et al. 2014; Sokół et al. 2015a) but are beyond the scope of this paper. Therefore, in reporting the He temperature, we adopt a philosophy based on our derivation from the complete sample but add the range of temperatures derived for different longitude selections as a systematic error contribution.

### 5.2.5. Combination of Uncertainties

So far, we have compiled systematic errors and uncertainties that affect the temperature determination for a fixed value  $V_{\text{ISN}\infty}$ . The compilation starts with a relatively small statistical fit uncertainty of about  $\pm 100$  K corresponding to about 1%.

Potential contributions of uncertainties in the sensor FOV and from trajectory deflection by the Earth are negligible. However, the observed trend of the derived temperature with observer longitude that may be attributed to a secondary ISN component and/or a non-thermal distribution is carried as a systematic error  $\Delta T_{\text{Syst}} = +430/-660$  K (see Figure 9). This is the largest uncertainty, which has to be added to the fit uncertainty along with the small correction for a potential magnetospheric contribution at the lower bound of the error bar in quadrature. Thus, for a center velocity  $V_{\text{ISN}\infty} = 26 \text{ km s}^{-1}$ , we obtain  $T_{\text{VISN}\infty} = 8710 + 440/-680$  K. In any comparison with temperatures derived from *Ulysses* observations (Witte 2004; Bzowski et al. 2014; Wood et al. 2015b), the temperature should be reported for the same fixed ISN flow velocity. Therefore, we have compiled such a comparison in Table 3, together with the center velocities and temperatures reported in the companion studies by Bzowski et al. (2015) and Schwadron et al. (2015). The uncertainties  $\Delta T_{\text{ISN}\infty}|V_{\text{ISN}\infty}$  quoted in Table 3 are solely those for fixed values of  $V_{\text{ISN}\infty}$ , i.e., only across the 4D parameter tube, which are usually substantially smaller than the total combined uncertainties derived below.

Except in comparison with the temperature given in Schwadron et al. (2015), which is taken from the 4D parameter tube in McComas et al. (2012) for the new value of  $V_{\text{ISN}\infty}$ , the temperature values from this study for  $V_{\text{ISN}\infty}$  quoted in the comparison studies are substantially higher than the best-fit temperatures quoted in the aforementioned papers. When going to the lower end of the uncertainty range, which is equivalent to attributing the entire systematic effect to the secondary component, the  $T_{\text{ISN}\infty}$  values that are obtained solely from the width of the latitude distributions come close to the values reported in Bzowski et al. (2015) for *IBEX* and in Bzowski et al. (2014) for *Ulysses*, with a remaining difference of about 500 K. Because the Warm Breeze contributes to the observed ISN flow distribution with a varying fraction over the entire longitude range, it may still influence the temperature derived

**Table 3**  
Comparison of ISN Temperatures from Different Studies

	Current <i>IBEX</i> Analysis			<i>Ulysses</i> Analysis	
	Schwadron et al. (2015)	Bzowski et al. (2015)	Witte (2004)	Wood et al. (2015b)	Bzowski et al. (2014)
$V_{\text{ISN}\infty}$ (km s $^{-1}$ )	25.4	25.9	26.4	26.08	26
$T_{\text{ISN}\infty}$ (K)	8010	7440	6300	7260	7500
$\Delta T_{\text{ISN}\infty}   V_{\text{ISN}\infty}$	$\pm 520$	$\pm 70$	$\pm 340$	$\pm 270$	$\pm 1500$
<b>This Study</b>					
$T_{\text{ISN}\infty} (V_{\text{ISN}\infty})$ (K)	8310	8580	8980	8760	8710
$\Delta T_{\text{ISN}\infty}   V_{\text{ISN}\infty}$	+410/−650	+430/−680	+450/−710	+440/−690	+440/−700

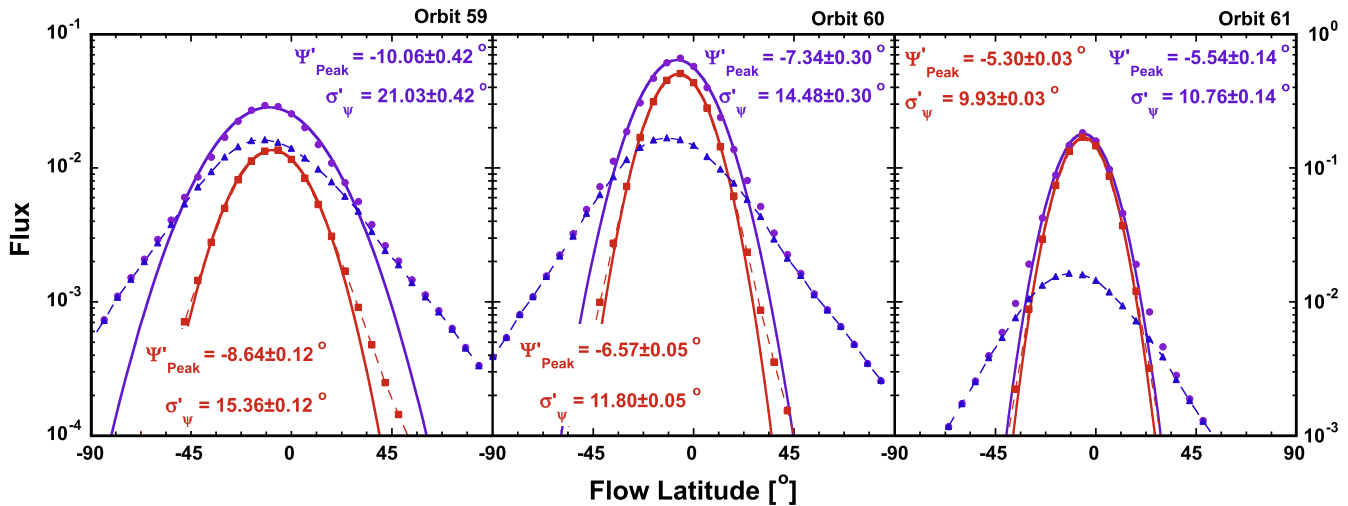


**Figure 11.** Modeled angular distributions for orbits 59 through 61 of the primary interstellar flow (squares) as obtained by Bzowski et al. (2012) and of the secondary He flow (triangles) as obtained by Kubiak et al. (2014) as best fits to *IBEX* observations, along with the combination of both (circles). The results of Gaussian fits to the combination and to the primary distributions are shown. It is obvious that contributions from the secondary population may substantially influence the peak location of the observed ISN flow distribution for orbits before orbit 61 and equivalent orbits. The deviation is already very small for orbit 61. However, the width of the distribution is still influenced more substantially.

in this study even for the largest observer longitudes. Then, the reported temperatures may be further corrected downward. However, the caveat is that using a  $\kappa$ -distribution instead of a Maxwellian may require a correction in the opposite direction.

To determine the full range of possible temperature values, uncertainties in the ISN flow speed also have to be propagated into the overall temperature uncertainty. The ISN flow speed affects the temperature uncertainty because, for a given observed width of the flow distribution, the temperature scales approximately with  $V_{\text{ISN}\infty}^2$ . The bulk flow longitude  $\lambda_{\text{peak}}$ , which connects  $\lambda_{\text{ISN}\infty}$  and  $V_{\text{ISN}\infty}$  through Equation (4.1), carries an uncertainty of  $\Delta\lambda_{\text{peak}} = 0.7^\circ$  which translates into  $\Delta V_{\text{ISN}\infty} = 0.5 \text{ km s}^{-1}$  for any deduced flow direction  $\lambda_{\text{ISN}\infty}$ . For a center velocity of  $V_{\text{ISN}\infty} = 26 \text{ km s}^{-1}$  and temperature of  $T_{\text{ISN}\infty} = 8710 \text{ K}$  from Table 3, this leads to an associated uncertainty of  $\Delta T_{\text{peak}} = \pm 330 \text{ K}$ . Adding these independent error contributions in quadrature, we report the temperature for a given flow longitude  $\lambda_{\text{ISN}\infty} = 75^\circ$  as  $T_{\text{ISN}\infty} = 8710 + 540/-740 \text{ K}$ .

Finally, the bounding range in  $\lambda_{\text{ISN}\infty}$  along the ISN parameter tube enters as a correlated temperature error. The range  $\lambda_{\text{ISN}\infty} = 75.6 \pm 1.4^\circ$  given by Schwadron et al. (2015) translates into the velocity range  $V_{\text{ISN}\infty} = 25.4 \pm 1.1 \text{ km s}^{-1}$  and leads to a bounding temperature range of  $7600 < T_{\text{ISN}\infty} < 9040 \text{ K}$ , which is subject to adding the previous uncertainties in quadrature.

## 6. SENSITIVITY OF ISN FLOW OBSERVATIONS TO SECONDARY EFFECTS AND LOCATION

We have discussed the substantial dependence of the derived temperature on observer longitude, which we have tentatively attributed to the influence of a secondary ISN flow population as found by Kubiak et al. (2014). In this section, we discuss how strongly such a distribution may affect both the ISN peak latitude and width, and thus the inferred ISN flow vector. This assessment also illuminates differences in the interpretation of the ISN flow between *Ulysses* and *IBEX* because these effects may differ with observer location.

### 6.1. Potential Influence by Secondary Neutral Atoms on the Observed ISN Flow

Kubiak et al. (2014) reported the first quantitative analysis of the secondary ISN population dubbed the Warm Breeze. They decomposed the observed He ISN flow distributions into two components, both drifting Maxwellian distributions at their assumed origin, i.e., at 150 AU upwind. While the primary ISN flow parameters were taken from Bzowski et al. (2012) for the core ISN flow observations in 2009 and 2010, the Warm Breeze parameters were fit to He distributions from orbits 54 through 68 in 2010.

In the following, we use the simulated data of these two ISN flow components as prepared with nWTPM to estimate the

influence of a secondary component on the ISN peak latitude and width as inferred from observations of the combined distributions. Figure 11 shows the primary ISN flow (squares), the Warm Breeze (triangles), and the combined distributions (circles) for orbits 59 through 61. Also shown are the resulting peak locations and widths obtained in fits to a Gaussian for the primary component (dashed line) and the combined distribution (solid line) for each orbit. The secondary component as extracted by Kubiak et al. (2014) shifts the peak location to noticeably larger negative latitude for orbits 59 ( $1^{\circ}4$ ) and 60 ( $0^{\circ}77$ ), with very little difference in orbit 61 (only  $0^{\circ}24$ ). For orbits later than 61 or equivalent, the difference in peak location is  $<0^{\circ}1$ , and thus below any of the uncertainties discussed in Section 3. To minimize the influence of the Warm Breeze on the analysis, only observations later than orbit 61 or at equivalent observer longitude are used for the ISN flow vector determination by Leonard et al. (2015) and Schwadron et al. (2015). Möbius et al. (2012) did include orbits 12, 60, and 61 in their analysis, which, along with the imperfection of the previous implementation of the aEXPM as discussed by Leonard et al. (2015), has likely contributed to moving the center value for  $\lambda_{\text{ISN}\infty}$  toward the larger longitude of  $79^{\circ}$  reported by Möbius et al. (2012).

Although the peak latitude is only slightly changed in orbit 61 by the Warm Breeze, the width of the distribution is affected more strongly. The width increase due to the presence of the secondary component is still 8.4%, which results in a substantial increase of the derived temperature by 17%. This result agrees with the observation in Figure 9 that the He temperature of 9140 K obtained for  $115^{\circ} < \lambda_{\text{Obs}} < 140^{\circ}$  appears to be higher by 13% than the value of 8050 K obtained for  $140^{\circ} < \lambda_{\text{Obs}} < 160^{\circ}$ . The broadening influence of a secondary component clearly decreases from smaller to larger observer longitude. Therefore, the varying contribution of the Warm Breeze to the ISN flow distribution is identified as a likely source for the observed trend in the derived He temperature. This finding has two important consequences. First, the influence on the width of the distribution may also have impacted the global  $\chi^2$  analysis using nWTPM (Bzowski et al. 2012), a possibility which we discuss next. Second, a full quantitative analysis of the ISN temperature that removes the systematic uncertainty quoted in Section 4.3 needs to include full consideration of the He secondary component in the comparative simulations.

To illustrate the effect that a hidden secondary component may have on the analysis of the ISN flow vector, Figure 12 shows the peak of the expected ISN flow distribution in latitude  $\psi'_{\text{Peak}}(\lambda_{\text{Obs}})$  and its width  $\sigma'_{\psi}(\lambda_{\text{Obs}})$  as a function of observer longitude  $\lambda_{\text{Obs}}$ , simulated with aEXPM. We have chosen a fixed ISN bulk flow location  $\lambda_{\text{Peak}}$ , but show three different flow directions in longitude  $\lambda_{\text{ISN}\infty}$  centered on the value obtained with *Ulysses* (Witte 2004). It is obvious from these curves that a model comparison with the *IBEX* observations can take advantage of the sensitivity to the variation of both observables to infer  $\lambda_{\text{ISN}\infty}$ . For larger  $\lambda_{\text{ISN}\infty}$  values, the peak latitude  $\psi'_{\text{Peak}}$  moves to more negative values and the width  $\sigma'$  increases more rapidly toward lower observer longitudes  $\lambda_{\text{Obs}}$ .

Inspecting the lower panel of Figure 12, we find that, compared with the curve for  $\lambda_{\text{ISN}\infty} = 75^{\circ}4$ , the variation of  $\sigma'_{\psi}$  with  $\lambda_{\text{Obs}}$  for  $\lambda_{\text{ISN}\infty} = 79^{\circ}0$  mimics the behavior of the observed width in Figure 9, which we simply attributed to a

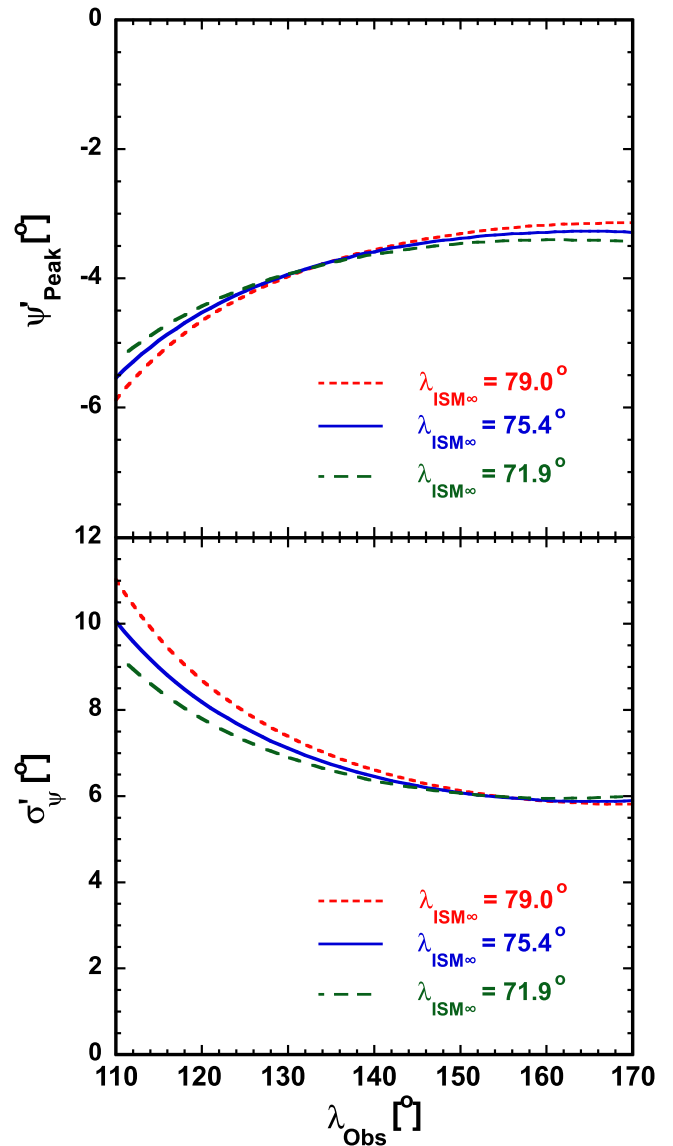


**Figure 12.** ISN peak latitude  $\psi'_{\text{Peak}}$  (top) and width  $\sigma'_{\psi}$  (bottom) as a function of observer longitude  $\lambda_{\text{Obs}}$  obtained with aEXPM. Shown are the model curves for a bulk flow peak location of  $\lambda_{\text{Peak}} = 130^{\circ}6$  and three different ISN flow longitudes at infinity. The variation in  $\lambda_{\text{ISN}\infty}$  leads to distinguishable curves in both observables.

secondary He component. If the analysis method is also sensitive to the width, then the presence of a secondary component will force the deduced flow longitude to larger values. The three-step method described here and used by Möbius et al. (2012), Leonard et al. (2015), and Schwadron et al. (2015) only uses the peak location in latitude, while the global  $\chi^2$  minimization used by Bzowski et al. (2012, 2015) includes the information of both observables simultaneously. Therefore, the three-step method is less sensitive to the variation of the width and other details in the ISN flow distribution when determining the ISN flow vector direction. It appears very likely that the center value  $\lambda_{\text{ISN}\infty} = 79^{\circ}2$  reported by Bzowski et al. (2012), based on the 2009 and 2010 ISN data, may partially be due to the still substantial influence of the secondary component on the width of the ISN flow in orbits where its impact on the peak latitude is already negligible, as discussed in Swaczyna et al. (2015).

By determining the temperature in a separate step after finding the flow vector in the three-step method, it becomes possible to separate effects in the distribution that indicate deviations from the original model assumptions, i.e., a single flow described by a Maxwellian distribution at infinity, more easily. The distinction between the variation of the peak location and width becomes important for the identification of potential effects from a secondary population and/or non-thermal distributions in the source populations. How exactly the width of the ISN flow varies from orbit to orbit, as shown in Figure 11, for example, is tied to the assumption of a Maxwellian for the Warm Breeze in the simulated data. Kubiak et al. (2014) explored a  $\kappa$ -distribution, which is the generalization of a Maxwellian to include other stationary states of the distribution, out of equilibrium (Livadiotis & McComas 2009, 2013). In such a case, the influence of the secondary component will decrease substantially more slowly with longitude.

### 6.2. Potential Location Dependence of the Secondary ISN Flow Distribution

When comparing the *IBEX* observations with *Ulysses*, the following question may arise. Why do the *IBEX* observations appear to be substantially more sensitive to the relatively weak secondary He component than those made with *Ulysses*? While *Ulysses* GAS is not sensitive enough to identify a small additional flow component of a few percent, as found with *IBEX* (Kubiak et al. 2014), the associated small shift and widening of the distribution would still apply. However, *Ulysses* observes the ISN flow from a variety of vantage points during its fast latitude scans, which allows a triangulation of the ISN flow vector, as used by Wood et al. (2015b). The *IBEX* analysis rests on variations of the peak latitude (three-step method) and the width (global  $\chi^2$  method) with observer longitude, both of which are affected by the secondary component.

In addition, as illustrated in Figure 13, the key part of the ISN flow distribution with the largest influence on the flow longitude determination with *IBEX* originates at the starboard flank of the heliospheric boundary. Zieger et al. (2013) indicated that the direction of the interstellar magnetic field, as deduced from the *IBEX* ribbon (Schwadron et al. 2009), from the termination shock asymmetry found by the *Voyagers* (Opher et al. 2007; Stone et al. 2008) and Ly $\alpha$  backscatter observations (Lallement et al. 2005, 2010) may lead to an asymmetry of the outer heliosheath, with substantially larger thickness on the starboard side. Consequently, the secondary component of ISNs may be noticeably stronger from the starboard side of the heliosphere compared with the nose and the port side. Conversely, *Ulysses* mainly samples ISN trajectories that stem from a narrow region around the nose. This difference may lead to a stronger influence of secondary neutrals on the ISN flow distribution observed by *IBEX*.

## 7. DISCUSSION AND CONCLUSIONS

In this paper, we have evaluated the ISN flow observations with *IBEX* and their analysis methods toward the ISN flow vector and temperature for underlying uncertainties and robustness against variations. This includes observational uncertainties in instrumentation, spacecraft, counting statistics, and potential differences in the simulations of the ISN flow, as

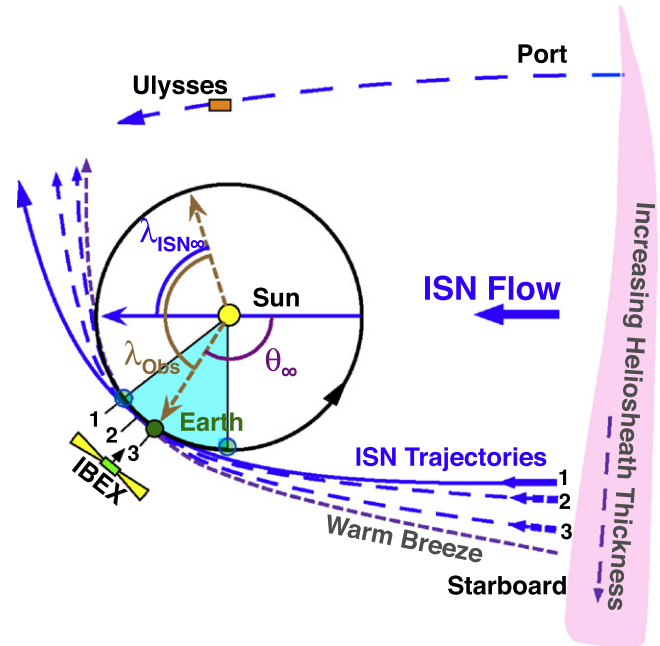


**Figure 13.** Schematic view of the interstellar flow observation for *IBEX* during spring in Earth orbit and for *Ulysses* during its fast latitude scans along with typical ISN flow and Warm Breeze trajectories from the outer heliosphere. The shaded section covers the range in  $\lambda_{\text{obs}}$  used with *IBEX* and the numbers indicate the sequence of trajectories sampled by *IBEX*.

well as influences from additional contributions to the ISN flow distribution due to a secondary component and consequences of the measurement location.

We have established an absolute pointing accuracy of the *IBEX*-Lo sensor, including sensor asymmetries and pointing relative to astronomical coordinates (Hlond et al. 2012), in latitude (or spin phase)  $\Delta\psi' = \pm 0^\circ.18$ , and in longitude  $\Delta\lambda = \pm 0^\circ.1$ . For ISN observations in the spring when the Earth moves into the oncoming ISN flow, any gravitational deflection for ISN trajectories passing the Earth before the observation is  $< 0^\circ.08$ , and thus smaller than any of the pointing uncertainties, while it may be substantially larger for fall observations (Kucharek et al. 2015). Related widening effects on the observed ISN flow distribution due to the pointing uncertainty and deflection by the Earth have a negligible influence on the derived temperature.

We have shown that in their current version, all four ISN flow simulation models in use for the *IBEX* ISN analysis, i.e., nWTPM, aWTPM, aFINM, and aEXPM, reproduce the ISN flow peak location in latitude as a function of observer longitude to better than  $0^\circ.1$  for the longitude range used in the analysis. The width of the distribution used to derive the temperature is reproduced by nWTPM, aWTPM, and aFINM to better than  $0^\circ.05$  over the entire longitude range. aEXPM reproduces the width at the location of the ISN bulk flow to within  $0^\circ.15$ , but shows deviations with increased width by up to  $0^\circ.5$ . Therefore, all four models can be used for the flow vector analysis and all but aEXPM for the temperature determination.

By employing the three-step method to determine the ISN flow parameters (Möbius et al. 2012) in an inter-model comparison, we have tested the robustness and sensitivity of the analysis to systematic and statistical uncertainties and shown the value of using different *IBEX* spin-axis orientations.

In particular, we find that the ISN flow vector is only minimally affected by the inclusion of ionization. The resulting flow longitude varies by  $<0^\circ.1$  for spin-axis orientations of  $\varepsilon_z = +0^\circ.7$  or  $\varepsilon_z = 0^\circ$  relative to the ecliptic plane and by  $<0^\circ.3$  for  $\varepsilon_z = -4^\circ.9$ , orientations that have been used thus far. While the knowledge of ionization is important for the correct determination of the bulk flow location where the typical He ionization rate changes the location by about  $0^\circ.5$  in longitude, its effects on the ISN flow vector direction are negligible. Because the flow vector determination builds on the  $V_{\text{ISN}\infty}(\lambda_{\text{ISN}\infty})$  relation found from the bulk flow longitude, we have tested how much the typical uncertainty of  $\pm 0^\circ.7$  in this location propagates into a flow vector uncertainty. We find that a related uncertainty of  $\Delta\lambda_{\text{ISN}\infty} < 0^\circ.1$  for  $\varepsilon_z = +0^\circ.7$  or  $\varepsilon_z = 0^\circ$  and  $\Delta\lambda_{\text{ISN}\infty} \leq 0^\circ.4$  for  $\varepsilon_z = -4^\circ.9$ . Thus, for a spin axis exactly in the ecliptic, which applies to about 50% of continuing *IBEX* observations, the uncertainties of the function  $V_{\text{ISN}\infty}(\lambda_{\text{ISN}\infty})$  and of the flow vector direction are completely independent. In a third test, we find that the newly established absolute pointing uncertainty of  $\pm 0^\circ.18$  in spin phase translates into an uncertainty for the flow longitude of  $\Delta\lambda_{\text{ISN}\infty} = \pm 1^\circ$  for  $\varepsilon_z = +0^\circ.7$  or  $\varepsilon_z = 0^\circ$  and  $\Delta\lambda_{\text{ISN}\infty} = \pm 0^\circ.7$  for  $\varepsilon_z = -4^\circ.9$ . The uncertainty in latitude is almost entirely controlled by the pointing uncertainty and, due to the frame transformation, translates into  $\Delta\beta_{\text{ISN}\infty} = \pm 0^\circ.28$ . In essence, the ISN flow vector direction is most sensitive to pointing uncertainties with leverage greater than a factor of 5 on  $\lambda_{\text{ISN}\infty}$ . Spin axis pointing to negative latitudes reduces this leverage by a factor of two.

After accounting for the difference in neutral trajectory tracking distance between nWTPM and aWTPM (to 150 AU) on one hand, for which the longitude of the ISN flow  $\lambda_{\text{ISN}\infty} = 76^\circ.15$  for  $\lambda_{\text{ISN}\infty, 150 \text{ AU}} = 75^\circ.4$ , and aFINM and aEXPM (to infinity) on the other hand, there are still some small, yet noticeable differences ( $<1^\circ$ ) in the derived longitudes. These differences are smaller than the uncertainties reported by Leonard et al. (2015) of  $\Delta\lambda_{\text{ISN}\infty} \pm 1^\circ.7$  and Schwadron et al. (2015) of  $\Delta\lambda_{\text{ISN}\infty} \pm 1^\circ.4$ . When adding noise to the simulated distributions according to Poisson statistics with typical accumulation times of a single *IBEX* orbit arc, we find that the inferred flow longitude varies with a standard deviation of  $\Delta\lambda_{\text{ISN}\infty} = \pm 1^\circ$  and may differ, for any single observation season, by a few degrees. Thus, the finding by Schwadron et al. (2015) that few single-year results show a standard deviation of  $\pm 2^\circ$  in  $\lambda_{\text{ISN}\infty}$  around the multi-year average and the value deduced for the data selection in Leonard et al. (2015) can be attributed in part to statistical variations. This surprisingly strong variation for an observation with a high signal-to-noise ratio is largely due to the strong leverage of any uncertainties or fluctuations in the latitude peak location on the flow longitude determination, as found for the pointing uncertainty in latitude. In conclusion, statistical uncertainties are substantial for small data sets, including entire single-year observations, but larger multi-year data sets lead to more accurate and robust results.

Therefore, it is important to expand the *IBEX* data set further. The pointing uncertainty will also be reduced further through more extended campaigns in the cross-calibration mode between the high- and low-resolution setting for entire orbit arcs, as already performed in 2015, which is not yet part of this analysis. In the future, simulated data sets with realistic Poisson noise will also be used effectively to study quantitatively the effects of the Warm Breeze and/or  $\kappa$ - versus Maxwell

distributions, both in the primary ISN flow and Warm Breeze, on results obtained with the three-step method and the global  $\chi^2$  minimization. Such an analysis is beyond the scope of this paper.

We have used aFINM (Schwadron et al. 2015) to obtain the ISN temperature from the width of the ISN distributions over the entire longitude range satisfying the selection criteria for the ISN analysis. We have simplified the analysis by scaling the width with  $\sqrt{T}$  after verifying that the results deviate by  $<1\%$  over the entire range for this parameterization. Before combining all of the data, we have corrected the 2009–2012 data sets for a small widening effect of  $<2.5\%$  in temperature due to limited data throughput across the *IBEX*-Lo-CEU interface (Möbius et al. 2015; Frisch et al. 2015). We have also verified that there is negligible contamination ( $\leq 2\%$  for the temperature) from potential magnetospheric foreground by comparing observations from ascending and descending orbit arcs. For the complete 2009–2014 data set, the inferred temperature is  $\approx 13\%$  higher in the observer longitude range  $115^\circ$ – $140^\circ$  compared with  $140^\circ$ – $160^\circ$ . By simulating the effect of an underlying wider angular distribution, we conclude that the most likely reason for the observed trend of increasing derived temperature for smaller observer longitude is the increasing contribution from the Warm Breeze (Kubiak et al. 2014).

We have studied this hypothesis further by comparing the best-fit primary ISN flow distributions with combined distributions that include the Warm Breeze as reported by Kubiak et al. (2014). The peak location is affected visibly up to longitudes equivalent to orbit 61 in 2010, but is negligible after that, which makes the contribution from the secondary component unimportant for the ISN flow vector determination based solely on the peak location as used by Leonard et al. (2015) and Schwadron et al. (2015) given the data selection for this analysis. However, Möbius et al. (2012) had included earlier orbits which likely contributed to their result of a larger center  $\lambda_{\text{ISN}\infty} = 79^\circ$ . The effect of the Warm Breeze on the width of the observed distributions is a substantial widening of the peak, even in the core ISN flow analysis orbits, which supports the conclusion that a variable contribution of the secondary component leads to the observed trend in the resulting temperature. The fact that the trend of the width with  $\lambda_{\text{Obs}}$  caused by the secondary component is akin to the effect of a larger ISN flow longitude, and that the global  $\chi^2$  minimization is not only sensitive to the peak location but also the width of the distributions, may have been a key reason for the central value of  $\lambda_{\text{ISN}\infty} = 79^\circ.2$  found by Bzowski et al. (2012). This inference agrees with the finding by Swaczyna et al. (2015) that the inclusion of the Warm Breeze in the analysis causes the largest difference in results and uncertainties.

We have discussed why *IBEX* observations are more sensitive to effects from the secondary component than *Ulysses* observations. In addition to the fact that *Ulysses* GAS images the ISN flow from a wide variety of vantage points along the *Ulysses* orbit (Wood et al. 2015b), *IBEX* views the major portion of the ISN flow distribution through the starboard side of the heliosphere relative to the oncoming ISN flow from its vantage point on the Earth orbit in spring, while *Ulysses* sees the ISN flow mostly from the nose and slightly to the port side. Models of the heliosphere (e.g., Zieger et al. 2013) suggest that the asymmetry due to the interstellar magnetic field direction as deduced from the *IBEX* ribbon and

the asymmetry of the termination shock may lead to a thicker outer heliosheath, and thus a more prominent secondary component coming from the starboard side of the heliosphere.

Overall, the distribution of the secondary component is not yet well characterized, and the ISN flow distribution may well be slightly non-thermal and better represented by a  $\kappa$  distribution, which would make the temperature derived using a Gaussian fit lower than in the interstellar medium. Therefore, we report an He temperature  $T_{\text{ISN}\infty} = 8710 + 440/-680$  K for a fixed ISN speed  $V_{\text{ISN}\infty} = 26$  km s<sup>-1</sup>, with the center value given by McComas et al. (2015a), in agreement with the earlier parameter tube (Bzowski et al. 2012; Möbius et al. 2012) when taking  $V_{\text{ISN}\infty} = 26$  km s<sup>-1</sup>. We include the trend in the derived temperature as a systematic error contribution, likely due to the varying contribution from the Warm Breeze. The most recent temperatures from *Ulysses* are also reported for  $V_{\text{ISN}\infty} = 26$  km s<sup>-1</sup> as  $T_{\text{ISN}\infty} = 7260 \pm 270$  K (Wood et al. 2015b) and  $T_{\text{ISN}\infty} = 7500 \pm 1500$  K (Bzowski et al. 2014). Even if we attribute the trend in  $T_{\text{ISN}\infty}$  with longitude solely to the Warm Breeze and adopt the lower end of the error bar as the ISN temperature, it is still 500–800 K higher than those reported from *Ulysses* as well as the temperature found by Bzowski et al. (2015) through global  $\chi^2$  analysis. At this point, it cannot be excluded that even for longitudes with the narrowest ISN distributions the influence of the Warm Breeze is not negligible, so that  $T_{\text{ISN}\infty}$  could be closer to the Bzowski et al. (2015) value. However, using a  $\kappa$ -distribution for the representation of the flow distribution may lead to a correction toward higher temperatures. In parallel, Wood et al. (2015a) have investigated whether a small hidden contribution of heavy neutrals, i.e., O and Ne, could lead to a lower derived *Ulysses* temperature. While they cannot rule out the possibility, they conclude that the contribution from this effect may only be minor.

Adding the uncertainty across the ISN parameter alley with  $\Delta\lambda_{\text{Peak}} = \pm 0.7$  and the related  $\Delta V_{\text{ISN}\infty} = \pm 0.5$  km s<sup>-1</sup> leads to  $T_{\text{ISN}\infty} = 8710 + 540/-740$  K for a fixed  $\lambda_{\text{ISN}\infty} = 75^\circ$ . Finally, we consider the bounding range along the parameter alley with  $\Delta\lambda_{\text{ISN}\infty} = \pm 1.4$  (Schwadron et al. 2015), which leads to a bounding range  $7600 < T_{\text{ISN}\infty} < 9040$  K for the central temperature value. As pointed out above, the contribution from the secondary component may be substantially different for both spacecraft locations, and we have not yet explored the potential effects of a genuinely non-thermal ISN distribution. The latter may affect the *Ulysses* observations with its lower S/N differently. While it is already clear that the ISN temperature is substantially higher than previously thought, a complete analysis of the ISN temperature awaits full consideration of the secondary component and non-thermal effects in the interstellar medium. On a large scale, it is already evident that the ISN gas is not strictly in thermal equilibrium because interstellar absorption lines, which represent line-of-sight averages over light years, clearly also contain a turbulent component in the observed line widths (e.g., Redfield & Linsky 2004). Refined analysis of the *IBEX* observations will be able to reveal whether and to what extent the local ISN velocity distribution contains non-thermal contributions in the form of a  $\kappa$  distribution, as may be expected for ion and neutral gas distributions with ongoing input from directed energy (Livadiotis & McComas 2013), for example, from flows or turbulence.

The authors are grateful to the many individuals at the *IBEX* co-investigator institutions who have made this project possible. This work is supported by the *Interstellar Boundary Explorer* mission as a part of NASA's Explorer Program and partially by NASA SR&T Grant NNG06GD55G, the Swiss National Science Foundation, PRODEX, and the Polish National Science Center grant 2012-06-M-ST9-00455.

## REFERENCES

- Adams, T. F., & Frisch, P. C. 1977, *ApJ*, 212, 300  
 Ajello, J. M. 1978, *ApJ*, 222, 1068  
 Bertaux, J., & Blamont, J. 1971, *A&A*, 11, 200  
 Bzowski, M., Kubiak, M., Hlond, M., et al. 2014, *A&A*, 569, A8  
 Bzowski, M., Kubiak, M., Möbius, E., et al. 2012, *ApJS*, 198, 12  
 Bzowski, M., Swaczyna, P., Kubiak, M. A., et al. 2015, *ApJS*, 220, 28  
 Frisch, P. C., Bzowski, M., Livadiotis, G., et al. 2013, *Sci*, 341, 1080  
 Frisch, P. C., Bzowski, M., Livadiotis, G., et al. 2015, *ApJ*, 801, 61  
 Funsten, H. O., Allegrini, F., Bochsler, P., et al. 2009, *SSRv*, 146, 75  
 Fuselier, S. A., & Cairns, I. H. 2013, *ApJ*, 771, 83  
 Fuselier, S., Bochsler, P., Chornay, D., et al. 2009, *SSRv*, 146, 117  
 Fuselier, S., Funsten, H., Heitzler, D., et al. 2010, *GeoRL*, 37, L13101  
 Galli, A., Wurz, P., Park, J., et al. 2015, *ApJS*, 220, 30  
 Gloeckler, G., Geiss, J., Balsiger, H., et al. 1992, *A&A*, 92, 267  
 Hlond, M., Bzowski, M., Möbius, E., et al. 2012, *ApJS*, 198, 9  
 Katushkina, O., Izmodenov, V. V., Wood, B., & McMullin, D. 2014, *ApJ*, 789, 40  
 Kubiak, M. A., Bzowski, M., & Sokół, J. M. 2014, *ApJS*, 213, 29  
 Kucharek, H., Galli, A., Möbius, E., et al. 2015, *ApJS*, 220, 35  
 Lallement, R., & Bertaux, J.-L. 2014, *A&A*, 565, A41  
 Lallement, R., Quemerais, E., Bertaux, J. L., et al. 2005, *Sci*, 307, 1447  
 Lallement, R., Quemerais, E., Koutroumpa, D., et al. 2010, in *AIP Conf. Proc.* 1216, 12th International Solar Wind Conf., ed. M. Maksimeric et al. (Melville, NY: AIP), 555  
 Lee, M., Kucharek, H., Möbius, E., et al. 2012, *ApJS*, 198, 10  
 Lee, M., Leonard, T., Möbius, E., et al. 2015, *ApJS*, 220, 23  
 Leonard, T., Möbius, E., Bzowski, M., et al. 2015, *ApJ*, 804, 42  
 Livadiotis, G., & McComas, D. J. 2009, *JGR*, 114, A11105  
 Livadiotis, G., & McComas, D. J. 2013, *SSRv*, 175, 183  
 McComas, D. J., Alexashov, D., Bzowski, M., et al. 2012, *Sci*, 336, 1291  
 McComas, D. J., Allegrini, F., Bochsler, P., et al. 2009, *SSRv*, 146, 11  
 McComas, D. J., Bzowski, M., Frisch, P., et al. 2015a, *ApJ*, 801, 28  
 McComas, D. J., Bzowski, M., Galli, A., et al. 2015b, *ApJS*, 220, 22  
 McComas, D. J., Carrico, J. P., Hautamaki, B., et al. 2011, *SpWea*, 9, S11002  
 Möbius, E., Bochsler, P., Bzowski, M., et al. 2009a, *Sci*, 326, 969  
 Möbius, E., Bochsler, P., Bzowski, M., et al. 2012, *ApJS*, 198, 11  
 Möbius, E., Bzowski, M., Chalov, S., et al. 2004, *A&A*, 426, 897  
 Möbius, E., Bzowski, M., Fuselier, S. A., et al. 2015, in *Proc. of the 13th AIAC* 577, *J. Phys.*, Conf. Ser. 012019, Voyager, IBEX, and the Interstellar Medium (Bristol: IOPP)  
 Möbius, E., Fuselier, S., Granoff, M., et al. 2008, in *Proc. of the 30th Int. Cosmic Ray Conf. 1*, ed. R. Caballero et al. (Universidad Nacional Autonoma de Mexico), 841  
 Möbius, E., Hovestadt, D., & Klecker, B. 1985, *Natur*, 318, 426  
 Möbius, E., Kucharek, H., Clark, G., et al. 2009a, *SSRv*, 146, 149  
 Opher, M., Stone, E. C., & Gombosi, T. 2007, *Sci*, 316, 875  
 Pogorelov, N. V., Heerikhuisen, J., Mitchell, J. J., et al. 2009, *ApJL*, 695, 31  
 Redfield, S., & Linsky, J. 2004, *ApJ*, 613, 1004  
 Saul, L., Wurz, P., Möbius, E., et al. 2012, *ApJS*, 198, 14  
 Scherer, K., & Fichtner, H. 2014, *ApJ*, 782, 25  
 Schwadron, N. A., Allegrini, F., Bzowski, M., et al. 2011, *ApJ*, 731, 56  
 Schwadron, N. A., Bzowski, M., Crew, G. B., et al. 2009, *Sci*, 326, 966  
 Schwadron, N. A., Lee, M., Möbius, E., et al. 2015, *ApJS*, 220, 25  
 Schwadron, N. A., Möbius, E., Kucharek, H., et al. 2013, *ApJ*, 775, 86  
 Smirnov, B. 1982, *Negative Ions* (New York: McGraw-Hill)  
 Sokół, J., Bzowski, M., Kubiak, M. A., et al. 2015a, *ApJS*, 220, 29  
 Sokół, J., Kubiak, M. A., Bzowski, M., et al. 2015b, *ApJS*, 220, 27  
 Stone, E. C., Cummings, A. C., McDonald, F. B., et al. 2008, *Natur*, 454, 71  
 Swaczyna, P., Bzowski, M., Kubiak, M. A., et al. 2015, *ApJS*, 220, 26  
 Thomas, G. E., & Krassa, R. F. 1971, *A&A*, 11, 218  
 Wahlström, P., Scheer, J., Wurz, P., Hertzberg, E., & Fuselier, S. 2008, *JAP*, 104, 034503-1  
 Weller, C., & Meier, R. 1974, *ApJ*, 193, 471

Wieser, M., Wurz, P., Möbius, E., et al. 2007, [RSci](#), **78**, 124502-1  
Witte, M. 2004, [A&A](#), **426**, 835  
Witte, M., Banaszkiewicz, M., & Rosenbauer, M. 1996, [SSRv](#), **78**, 289  
Wood, B., Mueller, H.-R., Bzowski, M., et al. 2015a, [ApJS](#), **220**, 31

Wood, B., Mueller, H.-R., & Witte, M. 2015b, [ApJ](#), **801**, 62  
Wurz, P., Saul, L., Scheer, J., et al. 2008, [JAP](#), **103**, 054904  
Zank, G. P., Heerikhuisen, J., Wood, B., et al. 2013, [ApJ](#), **763**, 20  
Zieger, B., Opher, M., Schwadron, N. A., et al. 2013, [GeoRL](#), **40**, 2923